SAND REPORT

SAND2002-2265
Unlimited Release
Printed July 2002

Final Report on LDRD Project: Development of Quantum Tunneling Transistors for Practical Circuit Applications

Jerry A. Simmons, Jeong-Sun Moon, Mark A. Blount, S. Ken Lyo, Wes E. Baca, John L. Reno, Mike P. Lilly, Joel R. Wendt, Mike C. Wanke, Xomalin G. Peralta, S. James Allen, James P. Eisenstein, and Peter J. Burke

Prepared by
Sandia National Laboratories
Albuquerque, New Mexico 87185 and Livermore, California 94550

Sandia is a multiprogram laboratory operated by Sandia Corporation, a Lockheed Martin Company, for the United States Department of Energy under Contract DE-AC04-94AL85000.

Sandia National Laboratories

Issued by Sandia National Laboratories, operated for the United States Department of Energy by Sandia Corporation.

Available to DOE and DOE contractors from
U.S. Department of Energy
Office of Scientific and Technical Information
P.O. Box 62
Oak Ridge, TN 37831

Telephone: (865)576-8401
Facsimile: (865)576-5728
E-Mail: reports@adonis.osti.gov
Online ordering: http://www.doe.gov/bridge

Available to the public from
U.S. Department of Commerce
National Technical Information Service
5285 Port Royal Rd
Springfield, VA 22161

Telephone: (800)553-6847
Facsimile: (703)605-6900
E-Mail: orders@ntis.fedworld.gov
Online order: http://www.ntis.gov/ordering.htm

SAND2002-2265
Unlimited Release
Printed July 2002

Final Report on LDRD Project: Development of Quantum Tunneling Transistors for Practical Circuit Applications

Jerry A. Simmons, Jeong-Sun Moon, Mark A. Blount, S. Ken Lyo,
Wes E. Baca, John L. Reno, and Mike P. Lilly
Semiconductor Material and Device Sciences Department

Joel R. Wendt and Mike C. Wanke
Photonic Microsystems Technology Department

Sandia National Laboratories
P. O. Box 5800
Albuquerque, New Mexico 87185-0601

Xomalin G. Peralta and S. James Allen
Department of Physics
University of California at Santa Barbara
Santa Barbara, California 90316

James P. Eisenstein and Peter J. Burke
Department of Condensed Matter Physics
California Institute of Technology
Pasadena, California 91125

Abstract

The goal of this LDRD was to engineer further improvements in a novel electron tunneling device, the double electron layer tunneling transistor (DELTT). The DELTT is a three terminal quantum device, which does not require lateral depletion or lateral confinement, but rather is entirely planar in configuration. The DELTT's operation is based on 2D-2D tunneling between two parallel 2D electron layers in a semiconductor double quantum well heterostructure. The only critical dimensions reside in the growth

direction, thus taking full advantage of the single atomic layer resolution of existing semiconductor growth techniques such as molecular beam epitaxy.

Despite these advances, the original DELTT design suffered from a number of performance shortcomings that would need to be overcome for practical applications. These included (i) a peak voltage too low (~20 mV) to interface with conventional electronics and to be robust against enviromental noise, (ii) a low peak current density, (iii) a relatively weak dependence of the peak voltage on applied gate voltage, and (iv) an operating temperature that, while fairly high, remained below room temperature.

In this LDRD we designed and demonstrated an advanced resonant tunneling transistor that incorporates structural elements both of the DELTT and of conventional double barrier resonant tunneling diodes (RTDs). Specifically, the device is similar to the DELTT in that it is based on 2D-2D tunneling and is controlled by a surface gate, yet is also similar to the RTD in that it has a double barrier structure and a third collector region. Indeed, the device may be thought of either as an RTD with a gate-controlled, fully 2D emitter, or alternatively, as a "3-layer DELTT," the name we have chosen for the device. This new resonant tunneling transistor retains the original DELTT advantages of a planar geometry and sharp 2D-2D tunneling characteristics, yet also overcomes the performance shortcomings of the original DELTT design. In particular, it exhibits the high peak voltages and current densities associated with conventional RTDs, allows sensitive control of the peak voltage by the control gate, and operates nearly at room temperature.

Finally, we note under this LDRD we also investigated the use of three layer DELTT structures as long wavelength (Terahertz) detectors using photon-assisted tunneling. We have recently observed a narrowband (resonant) tunable photoresponse in related structures consisting of grating-gated double quantum wells, and report on that work here as well.

Table of Contents

Purpose of LDRD Research 1

Background: Principle of Operation of the Two-Layer DELTT 2

Accomplishments 4

1. Growth, fabrication, and temperature measurements of high-temperature DELTTs with InGaAs notches 4
2. Development of a non-linear response theory of non-equilibrium 2D-2D tunneling 5
3. Demonstration of the three-layer DELTT, resulting in improved temperature performance, operating voltage, and gain 6
4. Development of a quantitative model for the electrical characteristics in a 3-layer DELTT 8
5. Increase of nearly four orders of magnitude in the current density of 3-layer DELTT devices 11
6. Observation of a resonant, tunable photoresponse in double quantum well layers 12
7. Speed measurements and partial development of a circuit model 12
8. Extended theory of photon assisted tunneling to include multiple photon events 13

Appendix I. List of Refereed Publications and Presentations 14

Refereed Publications 14

Presentations 15

Appendix II. "Double Barrier Resonant Tunneling Transistor With a Fully Two-Dimensional Emitter" 16

Appendix III. "Non-Equilibrium DC and Photon-Assisted Interlayer Tunneling in a Bi-Layer Tunneling Structure" 38

Appendix IV. "Photon-Assisted Transmission Through a Double-Barrier Structure" 44

Appendix V. "Terahertz Photoconductivity and Plasmon Modes in Double Well Field Effect Transistors" 49

Distribution 53

Final Report on LDRD Project:

Development of Quantum Tunneling Transisitors for Practical Circuit Applications

Project/Task Number: 10330.01

Responsible Project Manager: G. A. Samara, Org. 01120

Principle Investigators: J. A. Simmons, J. S. Moon, M. A. Blount, S. K. Lyo, W. E. Baca, J. L. Reno, J. R. Wendt, M. P. Lilly, M. C. Wanke, M. J. Hafich

Purpose of LDRD Research

At the time this LDRD was submitted in June of 1998, a team at Sandia led by the author had just recently demonstrated the Double Electron Layer Tunneling Transistor (DELTT). The DELTT is a three-terminal quantum transistor with excellent current isolation between input and output. This was the first three terminal quantum device which does not depend on lateral size confinement but rather was fabricated in an entirely planar manner. Thus it can be repeatably and reliably fabricated in the large numbers necessary for integrated circuits, using existing semiconductor processing techniques. This quality gives it a tremendous advantage over other proposed quantum transistors, such as those based on single electron charging.

At the start of this LDRD, DELTTs with excellent behavior at 77 K had been demonstrated, and models predicting the maximum operating temperature had been partially verified. In addition, circuits (bistable memories and digital logic gates) using the multifunctionality of the DELTT had also been demonstrated at 77 K. These latching NMOS-type SRAM memory cells utilized only one DELTT transistor, instead of the two necessary in conventional NMOS SRAM memory cells. Unfortunately, however, the DELTT suffered from a lack of voltage-gain; i.e. the voltage swing of the output was much smaller than the input signal needed to produce switching. This rendered the DELTT unsuitable for any signal processing or logic applications.

Because the DELTT is quantum, it should eventually be capable of extremely high speeds. In conjunction with its multifunctionality, this would make it particularly suited for such high-end applications as ultra-high speed A-to-D converters for use in radar imaging, and high speed transistors for communications. Before the DELTT can fully live up to its exceptional promise, however, a number of engineering obstacles need to be overcome. The most important of these are (1) modification of the growth structure so as to achieve room temperature operation, (2) engineering of the device geometry to reduce parasitics and thus achieve high speed, and (3) variations in design of the basic DELTT structure,

including additional layers, so as to achieve voltage gain.

The goal if this LDRD was to engineer further improvements in the DELTT so as to achieve room temperature operation, increase the operating speed, and assess the ultimate speed limitations. We pursued three different major thrusts. These were: (1) the use of different material systems with larger conduction band offsets than AlGaAs/GaAs so as to achieve deeper quantum wells and larger tunneling barriers for higher temperatures, (2) the design of DELTTs with very short low-capacitance gates, low-resistance channels, and various other optimized features designed to reduce parasitics and enable high speed, and (3) a redesign of the DELTT structure to include a third layer, enabling voltage gain.

Finally, we note under this LDRD we also investigated the use of three layer DELTT structures as long wavelength (Terahertz) detectors using photon-assisted tunneling. We have recently observed a narrowband (resonant) tunable photoresponse in related structures consisting of grating-gated double quantum wells, and report on that work here as well.

Background: Principle of Operation of the Two-Layer DELTT

A schematic of a completed DELTT structure is shown in Fig. 1. The source terminal makes electrical contact to the top QW only, while the drain terminal contacts the bottom QW only. These selective ohmic contacts to the individual QWs are formed by diffusing Au/Ge/Ni to *both* QWs, and then using a fixed DC bias on adjacent Ti/Au surface depletion gates in order to deplete electrons from the QW one does *not* wish to contact. An additional Ti/Au surface gate, placed between the depletion gates, acts as a third terminal and controls the tunneling.

In the DELTT, resonant tunneling can occur only when there exist states in both QWs

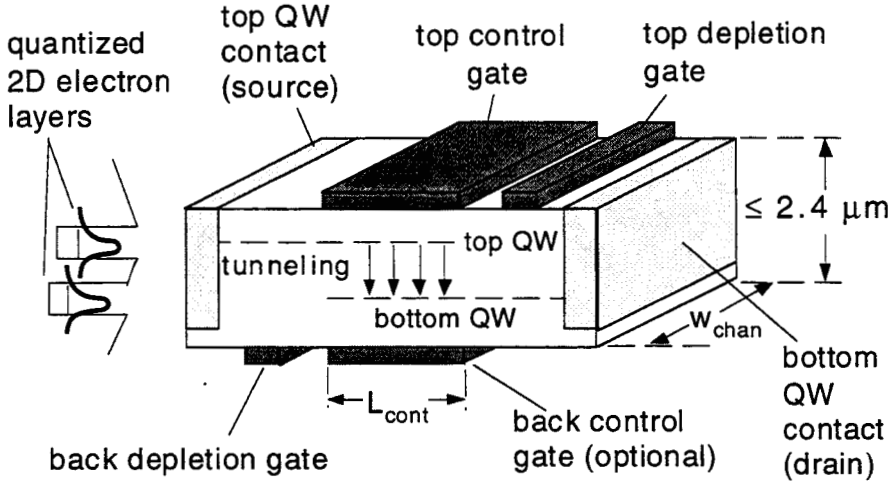

FIG. 1. Schematic of the double electron layer tunneling transistor (DELTT), not to scale. The source makes electrical contact to the top QW only, while the drain contacts the bottom QW only. The total thickness of the epitaxial layers ranges from 0.235 to 2.4 microns. w_{chan} is the width of the channel, and L_{cont} is the length of the control gate(s). A sketch of the DQW energy band diagram is shown at left.

with identical energy and in-plane momentum, since these quantities must be conserved in a 2D-2D tunneling event. (In this simple exposition of the operating principle we use the single-electron picture, and ignore inelastic events and electron-electron scattering.) One can determine when this condition is met by sketching the allowed states of the DQW in energy-momentum space, i. e. the dispersion curve.

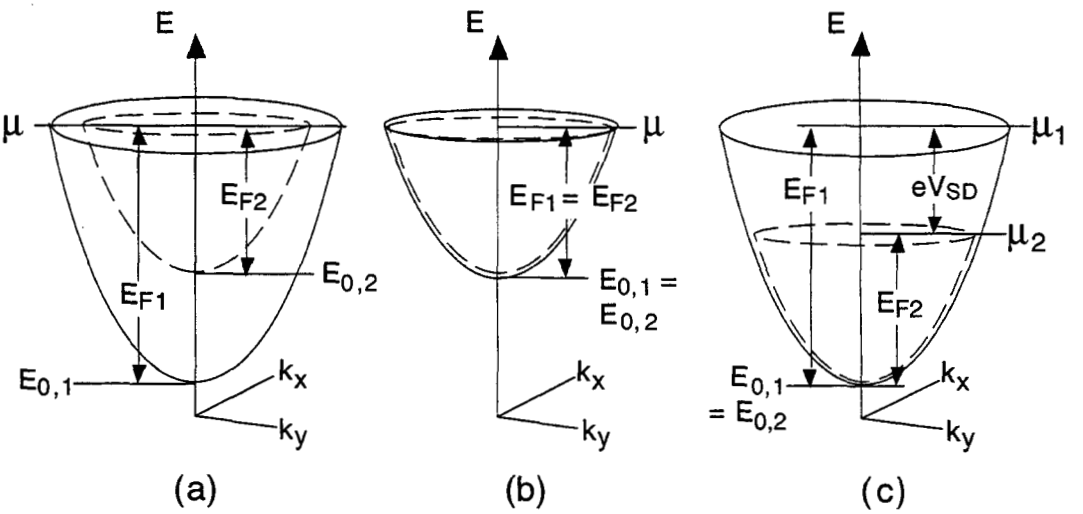

FIG. 2. Sketches of the allowed electron states of a DQW heterostructure in energy vs. in-plane momentum space, i. e. the dispersion curve. The two paraboloids have states only on the surface and none in the interior. (a) shows the case for a density-imbalanced DQW, with $V_{SD} = V_{TC} = 0$. Because no pairs of states of identical energy and momentum exist, tunneling cannot occur. In (b) V_{SD} remains at zero, but V_{TC} has been made sufficiently negative for the two paraboloids to coincide, allowing tunneling to occur. In (c) $V_{TC} = 0$, but V_{SD} has been increased so as to make the paraboloids coincide, again allowing tunneling current to flow.

Fig. 2(a) shows the dispersion of a DQW with a higher electron density in the top QW than in the bottom, at a top control gate voltage $V_{TC} = 0$, and a small applied source-drain bias $V_{SD} \approx 0$. Because both electron layers are 2D, their allowed states each form a paraboloid having states only on the surface, and none in the interior. While the chemical potentials $\mu_{1,2}$ of the two QWs coincide, their subband energies $E_{01,02}$ differ. Thus the paraboloids are offset in energy, no pairs of states of identical momentum and energy exist, and tunneling does not occur. Tunneling can be switched on by (1) varying the densities of either 2D layer with surface gates, (2) changing the chemical potential difference between the QWs by applying a source-drain bias, or (3) both. Fig. 2(b) shows the dispersion for the first case, when $V_{SD} \cong 0$ and the density of the top QW is decreased via a negative V_{TC} until it equals that of the bottom QW. (To first order, V_{TC} has no effect on the bottom QW until the top QW is completely depleted, since electrons in the QW effectively screen the electric field.) The two paraboloids then coincide, allowing tunneling to occur. This situation corresponds to a peak in the small-signal source-drain conductance G_{SD} as a function of V_{TC}. Fig. 2(c) shows the dispersion for the second case, when $V_{TC} = 0$ and eV_{SD} is increased to equal the difference in Fermi energy E_{F1}-$E_{F2} \equiv \Delta E_F$. Now the two

paraboloids again coincide; occupied states in the top QW are now paired with unoccupied states in the bottom QW at the same energy and in-plane momentum, and tunneling can occur. This situation corresponds to a peak in the source-drain current-voltage (I-V) curve. In general, the dispersion curves will coincide when

$$eV_{SD} - C_T V_{TC} \pi h^2/m^* = E_{F1} - E_{F2} = (n_1 - n_2)\pi h^2/m^* \quad (1)$$

where C_T is the capacitance per unit area between the top control gate and the top QW, m^* is the electron effective mass, and n_1 and n_2 are the electron densities in the two QWs. In the above we have assumed that the in-plane resistances of the two QWs are negligible in comparison to the tunneling resistance.

At this point the advantages of the DELTT over transistors based on DBRTDs, in which the tunneling is 3D-2D, are readily apparent: (1) the greater restriction in momentum states leads to sharper tunneling resonances, and (2) the density of each 2D layer can be easily controlled by surface gates, allowing an entirely planar device configuration.

ACCOMPLISHMENTS

Overall this was an extremely successful LDRD project. The most important result of the LDRD was the demonstration of a new device structure, incorporating three layers rather than the original two, which enabled voltage gain and operation at temperatures approaching 273 K, or 0 °C. For simplicity, we refer to this structure as the "three-layer DELTT." Below we enumerate our accomplishments , and describe them in more detail.

(1) Growth, fabrication, and temperature measurements of high-temperature DELTTs with InGaAs notches.

A series of conventional two-layer DELTT structures were simulated, grown, fabricated, and then measured. We tested the effect of various structure changes on the DELTT's operating temperature, with a view towards achieving room temperature operation. (Earlier we had verified that increasing the electron density raises the operating temperature significantly.) The structure changes involved (a) narrowing the well widths so as to push up the energy of the higher subbands and reduce the off-resonant valley current; (b) introducing InGaAs notches in the wells to deepen them and increase their quantum confinement, and (c) adding pure AlAs cladding layers adjacent to the wells to further increases the confinement and raise the higher subbands.

Fig. 3 shows the results of these measurements. Plotted as a function of temperature is the amplitude of the change in resistance between the tunneling resonance and the valley point, normalized to its value at 4 K. As can be seen, the first demonstrated DELTT structure (G1717) stops operating near 60 K, while the much higher density G1881 persists to considerably higher T. EA382, the narrow well sructure, performed slightly better than G1881. The addition of InGaAs notches (EA385) had a dramatic effect, causing the resonance to persist to much higher temperature. Surprisingly, the addition of AlAs cladding layers (EA381) actually caused the temperature performance to slightly decrease. This is believed to be due to a slight decrease in density due to the increased confinement.

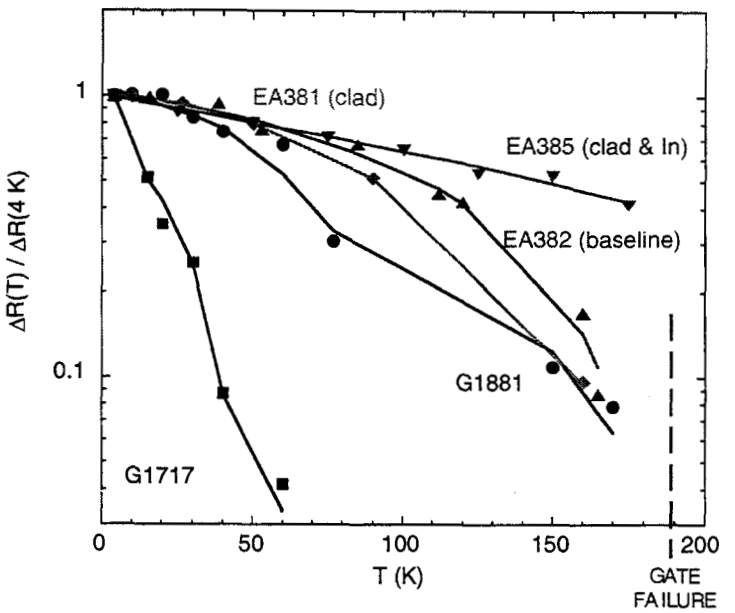

FIG. 3. Plot of normalized size of the tunneling resonance as a function of T for several samples. Sample with InGaAs notches in QWs shows best performance.

Unfortunately, an unexpected problem appeared. As indicated by the red line in Fig. 3, around 190 K the gates began to exhibit a slow drift in the bias points necessary for correct operation. The time constant of the drift decreased rapidly at higher temperatures, making it impossible to perform measurements. (Otherwise, it is likely that EA385 would've exhibited room temperature operation.) This drifting of the gate bias points is believed due to the thermal excitation of DX centers. As the DX center traps fill and/or empty, they screen the electric fields from the gate. It is believed that the problem might be reduced by a change in the Al content of the AlGaAs near the doping layers to 18 or 45 % from its present value of 30%, reducing the density of DX centers.

(2) Development of a non-linear response theory of non-equilibrium 2D-2D tunneling.

A theory for nonequilibrium 2D-2D tunneling between double electron layers with relatively large barriers was developed. The theory takes into account electron-impurity, electron-electron, and electron-phonon interactions. The theory is based on a rigorous second-order perturbative approach, and is exact to second order in the tunneling integral and to all orders in the interactions, and hence is highly useful for studying higher-order interaction effects which become important at high temperatures. Using it, we numerically evaluated, at several different temperatures, the source-drain I-V curves of a two-layer DELTT structure (G1881) which had previously been measured. Numerical results for T = 77 K are shown in Fig. 4. The theory shows good agreement with data source-drain biases below ~60 meV, where electrons begin to pass over the barriers induced by the depletion gates. However, numerical evaluations at 300 K still show a strong peak in the I-V curve, although the data does not. That G1881 shows no resonance at 300 K is likely due to problems with gate stability due to the thermal activation of DX centers, discussed

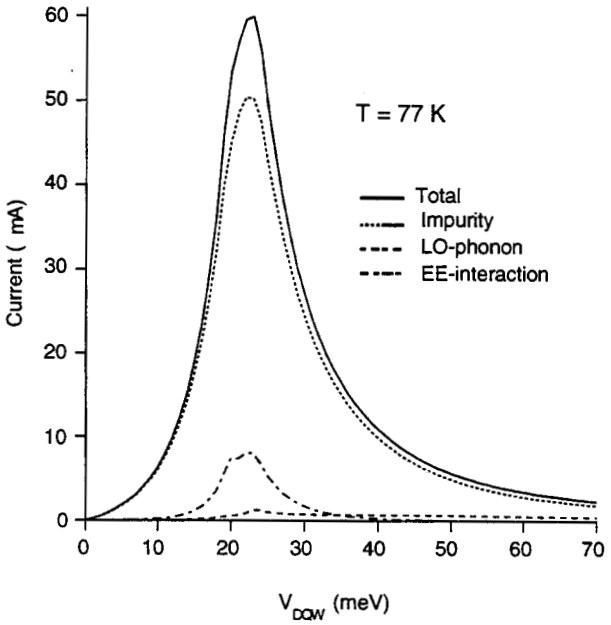

Fig. 4. Theoretical result for I-V curve of G1881 at 77 K, similar to measured data.

earlier. The important point is that theory predicts that strong 2D-2D tunneling resonances can persist up to room temperature.

(3) Demonstration of the three-layer DELTT, resulting in improved temperature performance, operating voltage, and gain

The original configuration of the DELTT involved a simple structure of two independently contacted QWs, with tunneling controlled by a surface gate. Two serious drawbacks to this device structure existed. (1) The source-drain voltage at which resonant tunneling occurs is limited to the difference in Fermi energies between the two wells, linearly proportional to their difference in 2D electron density. Because QWs can be doped to at most a density of a few times 10^{12} cm^{-2}, this limited the resonant source-drain voltage to a few 10s of mV. This is too low to be compatible with conventional electronics, and also makes the DELTT sensitive to environmental noise. (2) Because the control gate must be biased on the order of 100 mV to shift the quantum well Fermi energy by 10 meV, the two-layer DELTT configuration has a voltage gain of much less than unity.

We have now demonstrated a modified, three-layer DELTT structure, which spectacularly overcomes these difficulties. A sketch of the basic structure is shown in Fig. 5(a). In addition to the two quantum wells of the original structure, an additional third "collector" layer, sufficiently wide to be bulk-like, is added to the structure. Indeed, the structure can be thought of as an RTD with a gate-controlled, fully 2D emitter into which current is laterally fed. After an electron tunnels from the first quantum well to the second, it continues onward, tunneling through the second barrier and on into the continuum of states present in the wide collector layer. [See Fig. 5(b).] Because the second barrier is much thinner than the first, it is relatively transparent. The tunneling is thus still 2D-2D,

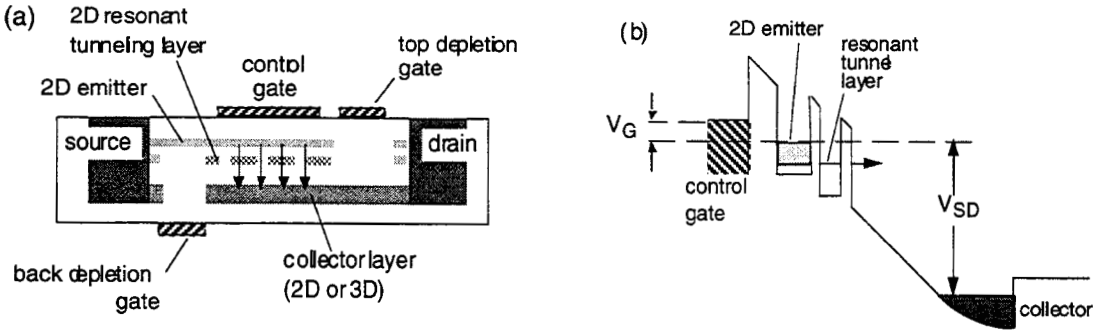

FIG. 5. (a) Sketched side-view of the 3-layer DELTT structure. (b) Band structure of the 3-layer DELTT. Electrons undergo 2D-2D tunneling, then continue through the second barrier into the continuum of states in the collector.

and retains the sharp characteristics of the two-layer DELTT devices. However, because a large voltage must be applied between the emitter and collector layers in order to get the emitter and resonant-layer subbands to align, the device can operate at source-drain voltages of order a few volts. Fig. 6 shows the source drain I-V curves of a three-layer DELTT structure, at different control gate biases. The resonant current peak occurs near 0.4 V, much larger than the few 10s of meV observed in two-layer DELTTs. For this test structure, the control gate was ~6500 Å from the emitter layer, and so greater than unity voltage gain was not found. With a 400 Å spacing as is typically found in HEMTs, a voltage gain greater than unity should be easily achievable.

An additional advantage of the three-layer structure is that the energy level of the

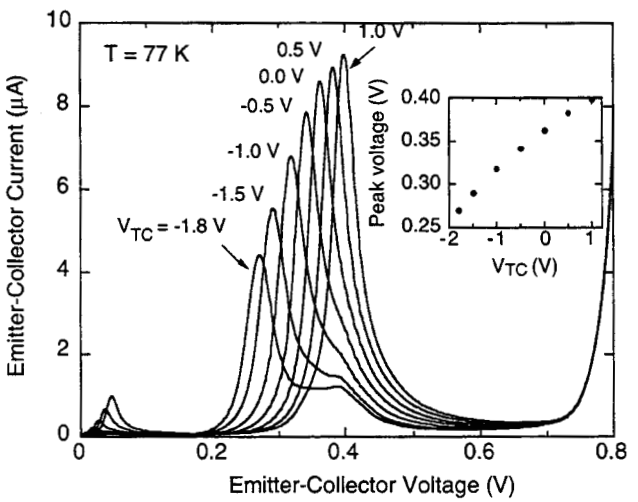

FIG. 6. Emitter-collector current vs. voltage of a device from the EA339 wafer, measured at 77 K for several values of V_{TC}. Inset shows how the peak voltage V_P changes as a function of control gate voltage V_{TC}.

resonant layer need not be occupied. This provides several advantages. First, the source-drain operating voltage can be made even larger, since the energy offset between the emitter and resonant subbands can be made much larger. This could also prove highly important for infrared detectors, allowing extension of the detected wavelength into the mid-IR. Second, the source-drain capacitance is now dramatically reduced, since the distance between the emitter and collector layers is now an order of magnitude or more larger than between the two quantum wells of the two-layer DELTT. This should improve the speed of the device.

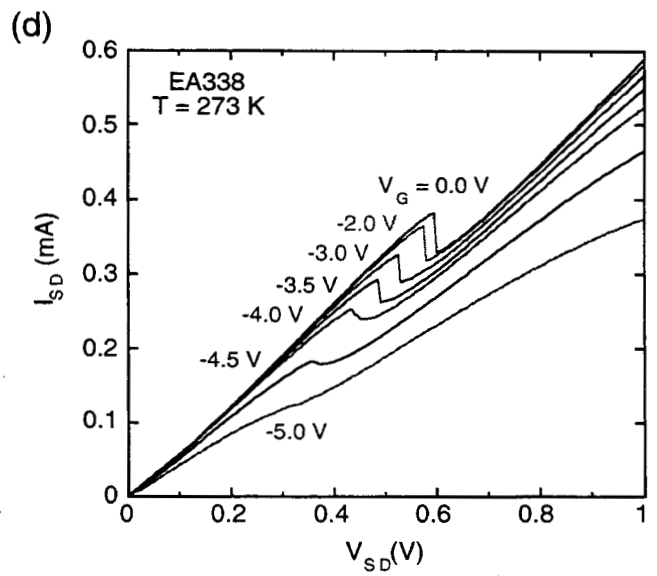

FIG. 7. Emitter-collector I-V characteristics of 3-layer DELTT EA338 at 273 K (0 °C) at several different gate voltages V_{TC}. Clear gate-control of the negative differential resistance is apparent, close to room temperature.

Finally, the three-layer DELTT operates at a much higher temperature than comparable two-layer DELTT structures. We believe that this is due to the additional energy-filtering provided by the second barrier, reducing the non-resonant valley current. Fig. 7 shows a set of source-drain I-V curves taken from EA338 at 0 °C. Although the negative differential resistance disappears by room temperature (300 K), we feel that our observation of NDR at *ice water temperatures* is highly promising, especially given that this structure was purely $Al_{0.3}Ga_{0.7}As/GaAs$. It now seems certain that true room temperature operation will be achieved shortly.

(4) Development of a quantitative model for the electrical characteristics in a 3-layer DELTT.

Previously we had demonstrated a 3-layer DELTT device, a substantial improvement over the original, two-layer DELTT: (1) The emitter collector voltage of the resonant tunneling current peak V_P was increased from a few 10s of mV up to order 1 V; (2) for reasons not completely understood, the operating temperature was substantially increased; and (3) the "resonant peak voltage gain" (G_{RPV}) increased substantially, The G_{RPV} is

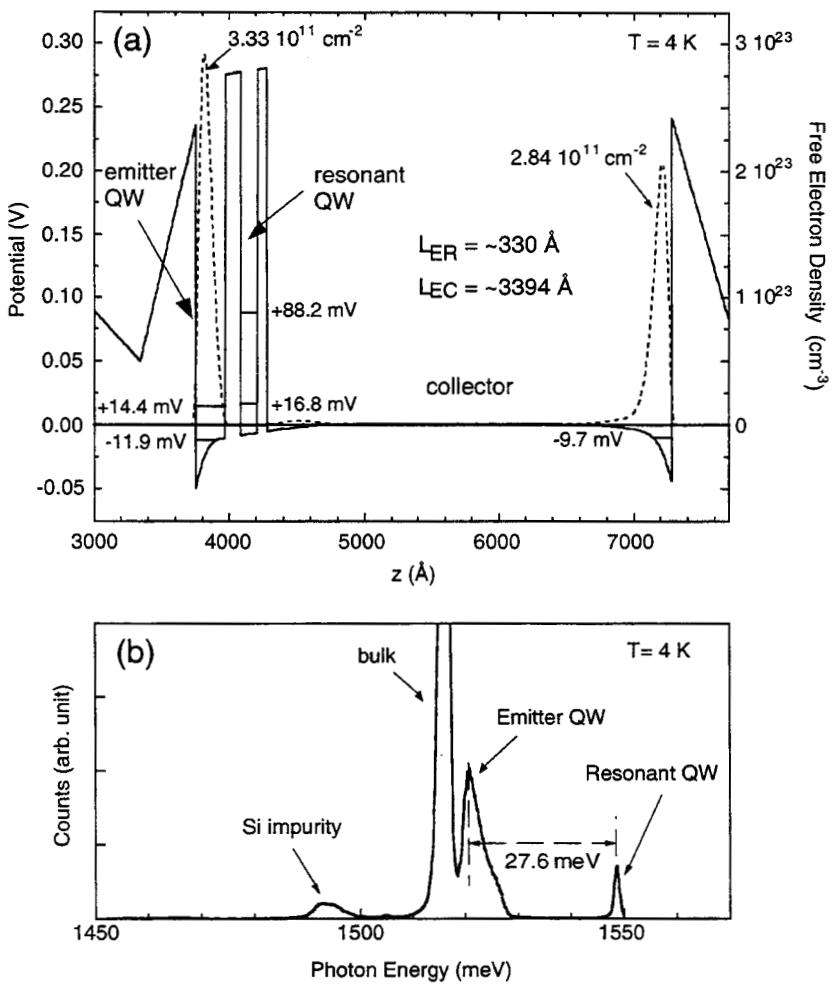

FIG. 8. (a) Results of an equilibrium self-consistent Hartree calculation of the band structure of 3-layer DELTT EA339. Zero energy represents the Fermi level. Significant free electron densities appear only in the emitter QW and at the far side of the collector. The energies of several subbands are indicated. The difference in energy between the emitter and ground subbands is 28.7 meV. (b) Photoluminescence data from wafer EA339. The difference in energy between the emitter and resonant QW ground subbands is 27.6 meV, close to the value obtained from the Hartree calculation.

defined as the change in the source-drain voltage at which the resonance occurs divided by the change in applied gate voltage, or $G_{RPV} = \Delta V_P/\Delta V_{TC}$.

This year we developed a quantitative model for values of V_P and G_{RPV}, given the growth structure parameters. Our model predicts that:

$$V_P = (L_{EC}/L_{ER})\Delta E_{ER}/e$$

and that

$$G_{RPV} = \Delta V_p / \Delta V_{TC} \approx \frac{\varepsilon}{d_{GE}} \frac{\pi \hbar^2}{m^* e^2} \frac{L_{EC}}{L_{ER}}$$

Here L_{EC} is the electron wavefunction separation between the emitter and collector subbands, L_{ER} is the wavefunction separation between the emitter and resonant layer subbands, ΔE_{ER} is the energy difference between emitter and collector subbands, and d_{GE} is the distance between the metallic control gate and the emitter.

To compare the model against the experimentally observed values, we used band structure parameters obtained both from self-consistent simulations of the 3-layer DELTT energy band diagram and from photoluminescence data. Fig. 8(a) shows a self consistent Hartee simulation of the energy band diagram of 3-layer DELTT structure EA339. Free

Device	L_{EB} (nm)	L_{CB} (nm)	V_P (V)	PVR (77 K)
EA339	12	8	0.36	32:1
EA338	10	8	0.50	20:1
EA491	8	8	0.65	15:1
EA492	7	7	1.40	3:1
EA493	6	6	1.63	1.1:1

Table 1. Device Parameters. L_{EB} is the emitter barrier thickness; L_{CB} is the collector barrier thickness; V_p is the emitter-collector voltage at the main resonance peak in the I-V; and PVR is the peak-to-valley current ratio.

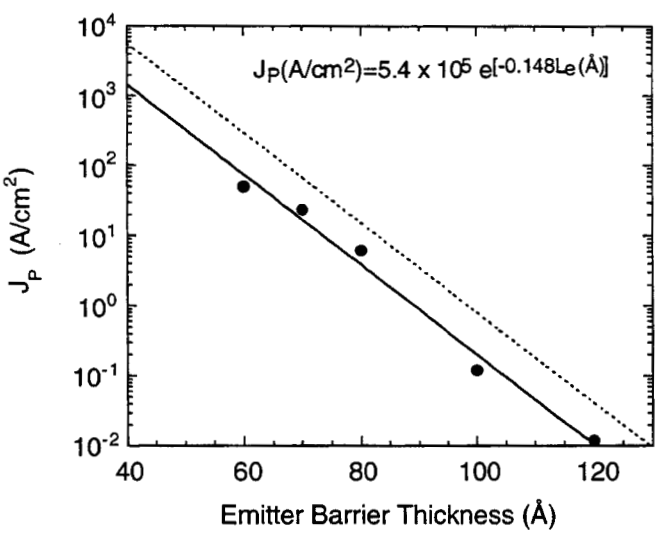

Fig. 9. Measured peak current density J_P vs. emitter barrier thickness L_{EB} for the devices in Table 1, which all had emitter densities of ~2.5 x 10^{11}. The solid line is a fit to the data. Extrapolation of the fit to a barrier thickness of 28 Å yields a current density of 8.2 x 10^3 A/cm^2, comparable to the higher values seen in RTDs. The dashed line represents the expected J_P for the case of an emitter QW with a density of 1x10^{12}/cm^2.

electrons (dotted line) accumulate only in the (left) emitter well and the far right region of the collector. L_{ER}, L_{EC}, and d_{GE} are obtained from the maxima in the respective wavefunctions. The simulation also yields the energies of the lowest subbands in the emitter and resonant layers. These are spaced apart by ΔE=28.7 meV. Similarly, Fig. 8(b) shows the photoluminescence from this structure. Peaks corresponding to the emitter QW and the resonant QW are clearly visible, and are separated in energy by ΔE=27.6 meV, close to the v Hartree simulation value.

Using these parameters in the model, we obtain values for wafer EA339 of V_P=0.30 V and G_{RPV}=0.044, which show fairly good agreement with the experimentally observed values of V_P=0.36 V and G_{RPV}=0.048. This verifies that the model is fairly accurate in predicting the electronic performance of the 3-layer DELTT. It can now be used in the design of future structures to maximize the gain and to choose the value and range of the resonant voltage V_P that is most desirable for a given application.

(5) Increase of nearly four orders of magnitude in the current density of 3-layer DELTT devices.

Although electron tunneling is extremely fast, in an actual device parasitic effects often limit the operating frequency long before the intrinsic switching speed is reached. Typically these take the form of an RC-like charging time $1/\tau = J_P/C_{EC}$, where C_{EC} is the capacitance between the emitter and collector. In any case, in order to realize extremely high speeds in the 3-layer DELTT, it is highly desirable to increase the peak current density, J_P.

In order to increase the current density, we grew a series of 3-layer DELTT structures in which the structure parameters were all kept constant except for the thickness of the two tunneling barriers, L_{EB} (emitter barrier thickness) and L_{CB} (collector barrier thickness), fabricated DELTT devices, and measured them at several different temperatures. These devices are shown in Table 1. The factors determining J_P are similar to those in RTDs. The first is the emitter barrier thickness. The relatively low J_P in EA339 is due to its extremely thick (d_{EB} = 120 Å) emitter barrier. The other structures, with thinner emitter barriers, have substantially larger J_P. Fig. 9 shows the J_P values measured at V_{TC} = 0 V from the five devices of Table 1, plotted as a function of d_{EB}. (These structures all have nominally the same emitter density of ~2.5 x 10^{11} cm^{-2}.) The peak current density J_P is seen to increase by a factor of ~1.52 for each monolayer (2.826 Å) reduction in L_{EB}. The current density of EA493, the highest, is nearly *four orders of magnitude larger* than EA339, the lowest. If the curve is extrapolated to a L_{EB} of only 10 monolayers (28.3 Å), then we would expect J_P to approach 8.2 x 10^3 A/cm^2.

The second factor influencing J_P is the supply function, or the number of emitter electrons available to participate in tunneling. The number of available emitter electrons per unit area is given by DOS(2D)*E_F^{2D}(emitter) = n_E^{2D}, the electron density in the emitter QW. Here DOS(2D) is the 2D electronic density of states, and E_F^{2D} (emitter) is the Fermi energy in the emitter. This is consistent with the increase in J_P with increasing V_{TC} observed in Fig. 6. [We note that in RTDs, a much weaker dependence on emitter density is found.] As a result, the current density of 3-layer DELTTs can also be substantially increased by raising the V_{TC} = 0 value of the emitter density. As indicated by the dashed line in Fig. 9, a 3-layer DELTT with a 1 x 10^{12} cm^{-2} emitter electron density and a L_{EB} = 10 monolayers can be expected to have J_P = 3.2 x 10^4 A/cm^2, comparable to some of the higher values reported for conventional RTDs. Because the emitter-collector capacitance per unit area C_{EC} of 3-layer DELTTs is also comparable to that found in RTDs, this new RTT device shows considerable promise for operating at comparable speeds of *several hundred GHz*.

(6) Observation of a resonant, tunable photoresponse in double quantum well layers.

Part of the way through this LDRD, we decided to pursue activities in an additional new direction. Due to the clear behavior of the 3-layer DELTT as a three terminal tunneling device, we had earlier suspected that it might exhibit an unusual photoconductance. Specifically, addition of a photon of the right energy might result in photon-assisted tunneling. Such a behavior could lead to a tunable, resonant photodetector in the sub-millimeter wave and terahertz regions of the spectrum. Some original work on this project had been pursued in a previous LDRD. In this LDRD, we followed up on a partucular configuration of such a detector, utilizing a grating gate on top of a double quantum well sample in which both wells were contacted in parallel.

This sample configuration, unlike the simple DELTT-like devices measured in the previous LDRD, exhibited an extremely sharp photoresponse in the THz regime. The peak in photocurrent could be tuned with the bias on the grating gate, and was actually sharper at higher temperatures, i.e. sharper at ~25 K than at 2 K. A simple model examining the energies of plasmon resonances in a partially depleted double quantum well sample is able to predict where the resonances occur, and agrees quite nicely with the data. However, the precise mechanism producing a photoresponse remains little understood. Details of this work appear in one of the appendices.

(7) Speed measurements and partial development of a circuit model.

We fabricated three-layer DELTTs in a special ground-signal-ground geometry designed for microwave probing for speed measurements. Devices had 100 micron wide and 1-10 micron long control gates. Measurements were performed in a cryogenic probe

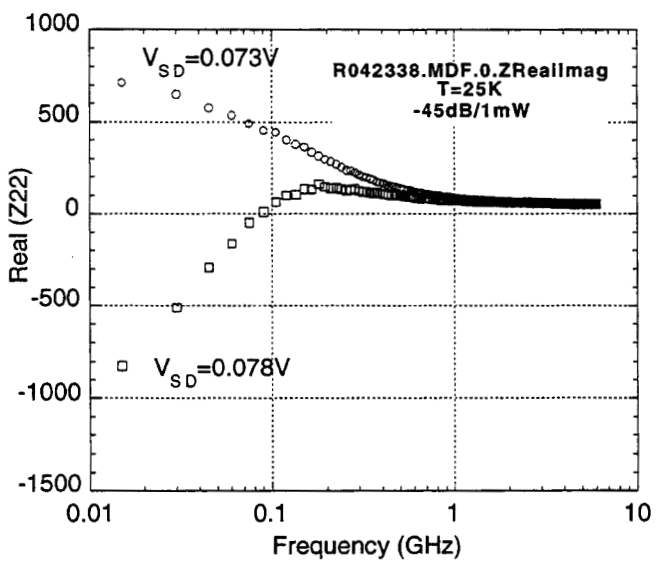

FIG. 10. Differential impedance vs. freq. in the negative differential resistance region (0.078 V) and off the negative differential resistance region (0.073 V).

station over 12 – 300 K. When the depletion gates were unbiased, so the device behaved like a conventional dual channel HEMT, a cut-off frequency of a quite respectable ~3 GHz and a maximum oscillation frequency of ~7 GHz was observed. With the depletion gates biased so the device was in the DELTT configuration, S-parameter measurements (see Fig. 10) indicate that the negative differential resistance survived to only 100 MHz. This is consistent with the very low source-drain current of these early 3-layer DELTT structures with thick tunneling barriers. We believe that the DELTT speed is currently limited by the RC charging time of the capacitance between the emitter and collector layers. By reducing the thickness of the tunneling barriers, we should be able to increase the speed of operation by roughly two orders of magnitude.

(8) Extended theory of photon assisted tunneling to include multiple photon events.

Finally, we note that under this LDRD we performed some work on the theory of photon-assisted tunneling, in an effort to better understand the behavior of these resonant plasmon double quantum well detectors. We studied the line shape of the non-equilibrium DC and photon-assisted tunneling current between two weakly tunnel-coupled electron layers as a function of DC bias energy and the temperature. The contributions from the intrinsic screened electron-phonon and electron-electron scattering to the widths of the tunneling peaks in the spectra were examined, and multiple photon events and higher subbands were included. Details can be found in the appendices.

APPENDIX I: List of Refereed Publications and Presentations

Refereed Publications:

1. Moon, J. S., J. A. Simmons, J. R. Wendt, V. M. Hietala, J. L. Reno, W. E. Baca, M. A. Blount, *Dual-Side Wafer Processing and Resonant Tunneling Transistor Applications,* Proceedings of the 1999 Joint International Meeting of SOTAPOCS XXXI, 10/17-22/99, Honolulu, HI.

2. Lyo, S. K., *Photon-Assisted Transmission through a Double-Barrier Structure,* Physical Review B **64**, 3311 (2001).

3. Khodier, M., C. Christodoulou, J. A. Simmons, *A THz Bowtie Antenna Coupled to a Tunable Double Quantum Well (DQW) Detector),*Proceedings of the 2001 IEEE AP-S International Symposium, 7/8-13/01, Boston, MA.

4. Khodier, M., C. Christodoulou, J. A. Simmons, *An Integrated Broadband Bowtie Antenna for THz Detection with a Double Quantum Well,* IEEE Transactions on Antennas and Propagation, submitted 5/01.

5. Khodier, M., C. Christodoulou, J. A. Simmons, *Equivalent Circuit Model for the Double Quantum Well (DQW) THz Detector,* IEEE Transactions on Electron Devices, accepted 5/02.

6. Lyo, S. K., J. A. Simmons, *Nonequilibrium DC and Photon-Assisted Interlayer Tunneling in a Bi-Layer Tunneling Structure,* Physica B **314**, 417 (2002).

7. Khodier, M. M., C. G. Christodoulou, J. A. Simmons, *A Bowtie Antenna Coupled Tunable Photon-Assisted Tunneling Double Quantum Well (DQW) THz Detector,* Proceedings of the 2001 Fall Meeting of the Materials Research Society, 11/26-30/01, Boston, MA.

8. Peralta, X. G., S. J. Allen, M. C. Wanke, N. E. Harff, J. A. Simmons, M. P. Lilly, J. L. Reno, W. E. Baca, P. J. Burke, J. P. Eisenstein, *Resonant Terahertz Photoconductance of Grating Gated Double Quantum Well Field Effect Transistors,* Proceedings of the Far-IR, Sub-MM and MM Detector Technology Workshop, 4/1-3/02, Monterey, CA.

9. Peralta, X. G., S. J. Allen, N. E. Harff, M. C. Wanke, M. P. Lilly, J. A. Simmons, J. L. Reno, P. J. Burke, J. P. Eisenstein, *Terahertz Photoconductivity and Plasmon Modes in Double Quantum Well Field Effect Transistors,* Applied Physics Letters, submitted 4/02.

10. J. S. Moon, J. A. Simmons, J. L. Reno, W. E. Baca, M. A. Blount, V. M. Hietala, E. D. Jones, *Double Barrier Resonant Tunneling Transistor With a Fully Two-Dimensional Emitter*, Applied Physics Letters, submitted 7/02.

Presentations:

1. Reno, J. L., J. A. Simmons, J. S. Moon, M. A. Blount, F. Gelbard, W. E. Baca, *Double Electron Layer Tunneling Transistor Modifications for Higher Temperature Operation,* North American Conference on Molecular Beam Epitaxy, 10/9-15/99, Banff, Alberta, CANADA.

2. Moon, J. S., J. A. Simmons, J. R. Wendt, V. M Hietala, J. L. Reno, W. E. Baca, M. A. Blount, *Dual-side Wafer Processing and Resonant Tunneling Transistor Applications,* 196th Electrochemical Society Meeting, 10/17-22/99, Honolulu, HI.

3. Simmons, J. A., *Terahertz Detection Based on Photon-Assisted Tunneling in Double Quantum Wells,* DARPA Terahertz Technology for Sensing and Satellite Communications Program Meeting, 11/2-3/99, Westlake Village, CA. (invited)

4. Lyo, S. K., J. A. Simmons, J. S. Moon, N. E. Harff, W. E. Baca, J. L. Reno, *Nonequilibrium Interlayer Tunneling in an Electron Bi-layer Structure,* March APS Meeting, 3/12-16/01, Seattle, WA.

5. Khodier, M., C. Christodoulou, J. A. Simmons, *A THz Bowtie Antenna Coupled to a Tunable Double Quantum Well (DQW) Detector,* 2001 IEEE AP-S International Symposium, 7/8-13/01, Boston, MA.

6. Lyo, S. K., J. A. Simmons, *Nonequilibrium DC and Photon-Assisted Interlayer Tunneling in a Double Electron Layer Tunneling Structure,* International Conference on Nonequillbrium Carrier Dynamics in Semiconductors, 8/27-31/2001, Santa Fe, NM.

7. Khodier, M., C. Christodoulou, J. A. Simmons, *A Bowtie Antenna Coupled Tunable Photon-Assisted Tunneling Double Quantum Well (DQW) THz Detector,* Fall Meeting of the Materials Research Society, 11/26-30/01, Boston, MA.

8. Peralta, X. G., S. J. Allen, M. C. Wanke, N. E. Harff, M. P. Lilly, J. A. Simmons, J. L. Reno, W. E. Baca, *Terahertz Photoconductivity and 2-D Plasmon Modes in Grating Coupled Double Quantum Wells,* March APS Meeting, 3/18-22/02, Indianapolis, IN.

9. Morath, C. P., M. P. Lilly, J. A. Simmons, J. L. Reno, W. E. Baca, J. S. Moon, *Temperature Dependence of Three-Layer Double Electron Layer Tunneling Transistor,* March APS Meeting, 3/18-22/02, Indianapolis, IN.

10. Peralta, X. G., S. J. Allen, M. C. Wanke, N. E. Harff, J. A. Simmons, M. P. Lilly, J. L. Reno, W. E. Baca, P. J. Burke, J. P. Eisenstein, *Resonant Terahertz Photoconductance of Grating Gated Double Quantum Well Field Effect Transistors,* Far-IR, Sub-MM & MM Detector Technolgy Workshop, 4/1-3/02, Monterey, CA.

Appendix II: "Double Barrier Resonant Tunneling Transistor With a Fully Two-Dimensional Emitter "

Double barrier resonant tunneling transistor with a fully two dimensional emitter

J. S. Moon*, J. A. Simmons, J. L. Reno, W. E. Baca, M. A. Blount, V. M. Hietala, and E. D. Jones.

Sandia National Laboratories, Albuquerque, New Mexico 87185-1415

A novel planar resonant tunneling transistor is demonstrated. The growth structure is similar to that of a double-barrier resonant tunneling diode (RTD), except for a fully two-dimensional (2D) emitter formed by a quantum well. Current is fed laterally into the emitter, and the 2D – 2D resonant tunneling current is controlled by a surface gate. This unique device structure achieves figures-of-merit, i.e. peak current densities and peak voltages, approaching that of state-of-the-art RTDs. Most importantly, sensitive control of the peak current and voltage is achieved by gating of the emitter quantum well subband energy. This quantum tunneling transistor shows exceptional promise for ultra-high speed and multifunctional operation at room temperature.

For well over two decades, electronic devices based on quantum effects have offered the promise of increased functionality and greatly enhanced switching speeds. Although various different devices have been proposed and demonstrated (*1-3*), to date the double barrier resonant tunneling diode (RTD) (*4,5*) based on tunneling from a three-dimensional (3D) emitter to a two-dimensional (2D) resonant layer, has been by far the most successful. RTDs have been demonstrated with resonant current peak-to-valley ratios (PVRs) of 30:1 at 300 K (*6*), picosecond switching times (*7*), and are now finding circuit applications in memories (*8,9*). RTD-like structures have also been shown to detect THz frequency photons (*10*). However, RTDs are only two terminal devices, which severely limits their usefulness and range of applications.

There have also been numerous attempts to develop a practical resonant tunneling transistor (RTT) by controlling the resonant tunneling current in RTDs via a base current (*11,12*) or a gate voltage (*13*). Such a three-terminal device would have many more applications than a conventional, two-terminal, RTD. By contrast, however, these efforts have met with much less success. (*14*) For instance, RTT's based on the side-wall gating of narrow RTD post-like structures (*13*) have suffered from relatively small transconductances, as well as severe fabrication problems due to the required submicron resolution and non-planarity of the geometry. The majority of these schemes to realize RTTs have involved slight modifications of the fundamental RTD design, which is based on 3D-2D tunneling. One early exception to this basic design was a planar structure involving the gate control of tunneling between a 3D and a 2D region through a single barrier. (*15,16*) Unfortunately, this device exhibited a very poor PVR, even at the low temperature of 7 K.

In the past few years, however, several techniques for making independent electrical contact to the two closely spaced (~200 Å) 2D electron layers in double quantum well (DQW) structures have been developed. (*17–19*) This has made possible the development of a new type of RTT, the double electron layer tunneling transistor (DELTT). In this device, resonant tunneling occurs between *two independently contacted 2D electron layers* separated by *a single barrier*, and is controlled by a surface gate. (*20-22*) The DELTT represented a significant advance over other RTTs, as it exhibited PVRs of order 10:1 at 77 K, was sufficiently stable to act as a single transistor static memory, and enabled the demonstration of unipolar complementary circuits for the first time. (*23*) Most importantly, the DELTT geometry is entirely planar and scalable, meaning that in principle it could be used in large numbers in integrated circuits. Despite these advances, the original DELTT design suffered from a number of performance shortcomings that would need to be overcome for practical applications. These included (i) a peak voltage too low (~20 mV) to interface with conventional electronics and to be robust against enviromental noise, (ii) a low peak current density, (iii) a relatively weak dependence of the peak voltage on applied gate voltage, and (iv) an operating temperature that, while fairly high, remained below room temperature.

In this article, we report an advanced resonant tunneling transistor that incorporates structural elements both of the DELTT and of conventional double barrier RTDs. Specifically, the device is similar to the DELTT in that it is based on 2D-2D tunneling and is controlled by a surface gate, yet is also similar to the RTD in that it has a double barrier structure and a third collector region. Indeed, the device may be thought of either as an RTD with a gate-controlled, fully 2D emitter, or alternatively, as a "3-layer

DELTT," the name we have tentatively chosen for the device. As we demonstrate here, this new RTT retains the original DELTT advantages of a planar geometry and sharp 2D-2D tunneling characteristics, yet also overcomes the performance shortcomings of the original DELTT design. In particular, it exhibits the *high peak voltages and current densities* associated with conventional RTDs, allows *sensitive control of the peak voltage* by the control gate, and operates nearly at *room temperature.*

We now turn to the basic design and operation of the new 3-layer DELTT. Fig. 1(a) shows a sketch of the band structure, and Fig. 1(b) a cross sectional view of the device geometry. Current flows from the emitter to the collector as follows: First, electrons are fed laterally from the emitter contact into the lowest 2D subband of the emitter QW. If the gate is biased appropriately, the electrons then tunnel vertically through the emitter barrier into the lowest 2D subband of the resonant layer QW. Once electrons are in the resonant layer QW, they will then continue onwards through the much thinner collector barrier, into the broad continuum of electron states existing in the third bulk-like collector layer. (*24*) The electrons then flow laterally through the collector layer into the collector contact, exiting the device. (*25*) A significant impediment to current flow can exist only when electrons tunnel from the emitter subband to the resonant layer subband. As in the case of the original double quantum well DELTT, this 2D-2D tunneling step can only occur when these two subbands are precisely aligned in energy, due to the simultaneous conservation of energy and momentum. (*20*) The subbands can be brought into alignment by either (i) applying sufficient emitter-collector bias, or (ii) biasing the control gate to raise or lower the emitter subband energy, or (iii) both.

The 3-layer DELTT devices described in this work were processed from several different molecular beam epitaxy (MBE) grown GaAs/$Al_{0.3}Ga_{0.7}As$ heterostructures, whose parameters are given in Table 1. For all devices, the emitter QW was 220 Å thick and the resonant QW 120 Å thick. The GaAs collector layer was 3000 Å thick for all structures except EA338, for which it was 2000 Å. The emitter and collector barrier thicknesses (L_{EB} and L_{CB}) were varied over a wide range, subject to the constraint $L_{CB} \leq L_{EB}$. Independent contacts to the emitter and collector layers were formed by biasing (typically at a few volts) front and back depletion gates to deplete electrons from all layers except the contacted one. (*17*) The close proximity backgates were only ~0.5 μm from the collector layer, and were fabricated using the epoxy-bond-and-stop-etch (EBASE) process. (*19*) The typical lateral dimensions of the gates and their spacings are similar to those of the original DELTT structures, described earlier. (*20*) All measurements exhibited excellent reproducibility over thermal cycling.

In Fig. 2 we show the 77 K emitter-collector current-voltage (I-V) characteristics of 3-layer DELTT EA339, for several top control gate voltages V_{TC}. The I-V is highly non-linear, with sharp resonant tunneling peaks whose current and voltage positions are clearly controlled by V_{TC}. Strikingly, at $V_{TC} = 0$ the main resonant peak voltage V_P is at $V_{EC} \approx 0.36$ V, over an order of magnitude larger than typically observed in 2-layer DELTTs. (*21*) In addition, the peak-to-valley ratio at $V_{TC} = 0$ is 32:1, which is also considerably higher than observed in 2-layer DELTTs at this temperature. As V_{TC} increases (i.e. as the Fermi energy in the emitter QW increases), both the peak current density J_p and the peak voltage V_P increase monotonically.

A quantitative understanding of this high V_P can be gained with the following simple model. If the applied emitter-collector bias V_{EC} is assumed to drop uniformly across the distance L_{EC} between the electron wavefunctions of the emitter and collector [see Fig. 1(a)], then we expect that:

$$V_P = (L_{EC}/L_{ER})\Delta E_{ER}/e \qquad (1)$$

where L_{ER} is the distance between the electron wavefunctions of the emitter and resonant layer subbands, and $\Delta E_{ER} = E_{R0}-E_{E0}$ is the difference in energy between the emitter and resonant layer ground subbands at zero bias. Fig. 3(a) shows the results of a 4.2 K self-consistent Hartree calculation of the bandstructure of EA339 at $V_{TC} = V_{EC} = 0$. From this we obtain ΔE_{ER} = 28.7 meV, L_{EC} = 3394 Å, and L_{ER} = 330 Å. This yields an estimate of V_P = 0.30 V, in fair agreement with the observed value. This calculated value for ΔE_{ER} is further supported by photoluminescence (PL) measurements on wafer EA339, shown in Fig. 3(b). The emitter and resonant QW peaks are clearly visible in the PL data, and their energy difference of 27.6 meV is close to our calculated value. (*26,27*)

The increase in V_P with increasing V_{TC} is further illustrated in the inset to Fig. 2. We define the resonant peak voltage gain G_{RPV} as $\Delta V_P/\Delta V_{TC}$, which provides a useful measure of the effectiveness of the gate. A value for G_{RPV} can be estimated from our model by assuming that the gate acts only to change the electron density in the emitter, and that any electric field penetration from the gate to the collector layer is negligible. (23) Thus we obtain:

$$G_{RPV} = \Delta V_p / \Delta V_{TC} \approx \frac{\varepsilon}{d_{GE}} \frac{\pi \hbar^2}{m^* e^2} \frac{L_{EC}}{L_{ER}} \qquad (2)$$

where ε is the dielectric constant, d_{GE} is the gate to emitter wavefunction distance, and m* is the effective mass. Using m* = 0.067 m_e, d_{GE} = 6000 Å, and the L_{EC} and L_{ER} values obtained from the Hartree simulation for V_{TC} = 0, we obtain $\Delta V_P / \Delta V_{TC}$ = 0.044, quite close to the experimental value of ~ 0.048 at V_{TC} = 0. This measured value for G_{RPV} is rather small because of the unusually large gate-emitter distance d_{GE} of 6000 Å for this test structure, which contained a silicon oxide layer beneath the gate. We expect that 3-layer DELTT structures with d_{GE}'s approaching the 500 Å typically found in commercial HEMTs should readily exhibit a G_{RPV} of unity or above. Nonetheless, the data amply illustrate that the G_{RPV} is increased by the geometric leverage factor L_{EC}/L_{ER} (> 10) over that observed in the previous DQW DELTT. Thus, unity G_{RPV} operation, which is extremely difficult to obtain from a single barrier tunneling device (*15,16,20*) can be readily achieved in these new 3-layer DELTT structures.

We now turn to the subject of current density J_P in the 3-layer DELTT. Although the intrinsic speed of electron tunneling is extremely fast, in an actual device parasitic effects often limit the operating frequency long before the intrinsic switching speed is reached. Typically these take the form of an RC-like charging time $1/\tau = J_P/C_{EC}$, where C_{EC} is the capacitance between the emitter and collector. (*28*) Thus, in order to realize extremely high speeds in the 3-layer DELTT, it is highly desirable to increase the peak current density, J_P.

The factors determining the current density in the new 3-layer DELTTs are similar to those in RTDs. The first factor determining J_P is the emitter barrier thickness. The relatively low J_P in EA339 is due to its extremely thick (d_{EB} = 120 Å) emitter barrier. The

other structures, with thinner emitter barriers, have substantially larger J_P. Fig. 4 shows the J_P values measured at $V_{TC} = 0$ V from the five devices of Table 1, plotted as a function of d_{EB}. (These structures all have nominally the same emitter density of ~2.5 x 10^{11} cm^{-2}.) The peak current density J_P is seen to increase by a factor of ~1.52 for each monolayer (2.826 Å) reduction in d_{EB}. (*29*) If the curve is extrapolated to a d_{EB} of only 10 monolayers (28.3 Å), then we would expect J_P to approach 8.2 x 10^3 A/cm^2.

The second factor influencing J_P is the supply function, or the number of emitter electrons available to participate in tunneling. The number of available emitter electrons per unit area is given by $DOS(2D)*E_F^{2D}(emitter) = n_E^{2D}$, the electron density in the emitter QW. Here DOS(2D) is the 2D electronic density of states, and E_F^{2D} (emitter) is the Fermi energy in the emitter. This is consistent with the increase in J_P with increasing V_{TC} observed in Fig. 2. [We note that in RTDs, a much weaker dependence on emitter density is found, $DOS(2D) \cdot E_F^{3D}(emitter) = \frac{\pi}{2}\left(\frac{3n_E^{3D}}{\pi}\right)^{2/3}$.] As a result, the current density of 3-layer DELTTs can also be substantially increased by raising the $V_{TC} = 0$ value of the emitter density. As indicated by the dashed line in Fig. 4, a 3-layer DELTT with a 1 x 10^{12} cm^{-2} emitter electron density and a d_{EB} = 10 monolayers can be expected to have J_P = 3.2 x 10^4 A/cm^2, comparable to some of the higher values reported for conventional RTDs. Because the emitter-collector capacitance per unit area C_{EC} of 3-layer DELTTs is also comparable to that found in RTDs, this new RTT device shows considerable promise for operating at comparable speeds of several hundred GHz.

Finally, we discuss the temperature behavior of 3-layer DELTTs. Fig. 5(a) shows the emitter-collector I-V curve of DELTT EA339 at $V_{TC} = 0$ V, for several temperatures.

While below 200 K the valley current increases relatively slowly with, a sudden increase in valley current above ~200 K results in a diminished PVR. Nonetheless, regions of NDR persist to ~250 K. Similar behavior is also observed for DELTT EA338, which is shown in Fig. 5(b) for several different V_{TC} at 273 K, or 0 °C. Clear gate control of the resonant current peak is observed. We note that these 3-layer DELTTs operate at temperatures considerably higher than the original DQW DELTTs. We attribute this to the double barrier structure of the new design, which serves to reduce the off-resonant valley current. Because the new 3-layer DELTT structure shares the double-barrier design of RTDs, we expect that room temperature operation can be achieved via the use of different material systems with higher conduction band offsets, much as has been observed in RTDs. Such material systems would include, for instance, $In_{0.53}Ga_{0.47}As/In_{0.52}Al_{0.48}As$ lattice matched to InP (*6,30*), or InAs/AlSb/GaSb (*31*).

In summary, we have demonstrated a new resonant tunneling transistor which combines the novel gate-controlled 2D-2D tunneling mechanism of the original DELTT transistor with the resonant double-barrier structure found in conventional RTDs. The resulting RTT is fully planar, and exhibits operation at high temperatures, high peak voltages, and high current densities, holding excellent promise for further development as a practical high-speed electronic device.

References

* Present Address: RL61B, Hughes Research Laboratories, 3011 Malibu Canyon Rd., Malibu, CA 90265.

1. A. O. Orlov, I. Amlani, G. H. Berstein, C. S. Lent, G. L. Snider, Science **277**, 928 (1997).

2. L. J. Guo, E. Leobandung, S. Y. Chou, Science **277**, 21 (1997).

3. S. J. Tans, A. R. M. Verschueren, C. Dekker, Nature **393**, 49 (1998).

4. R. Tsu, L. Esaki, Appl. Phys. Lett. **22**, 562 (1973).

5. L. L. Chang, L. Esaki, R. Tsu, Appl. Phys. Lett. **24**, 593 (1974).

6. T. P. E. Broekaert, W. Lee, C. G. Fonstad, Appl. Phys. Lett. **53**, 1545 (1988).

7. J. F. Whitaker, G. A. Mourou, T. C. L. G. Sollner, W. D. Goodhue, Appl. Phys. Lett. **53**, 385 (1988).

8. P. Mazumder, S. Kulkarni, M. Bhattacharya, J. P. Sun, G. Haddad, Proceedings of the IEEE. **86**, 664 (1998).

9. J. P. A. Vanderwagt, A. C. Seabaugh, E. A. Beam, IEEE Electron Dev. Lett. **19**, 7 (1998).

10. H. Drexler, J. S. Scott, S. J. Allen, K. L. Campman, A. C. Gossard, Appl. Phys. Lett. **67**, 2816 (1995).

11. F. Capasso, R. A. Kiehl, J. of Appl. Phys. **58**, 1366 (1985).

12. M. A. Reed, W. R. Frensley, R. J. Matyi, J. N. Randall, A. C. Seabaugh, Appl. Phys. Lett. **54** , 1034 (1989).

13. W. B. Kinard, M. H. Weichold, W. P. Kirk, J. Vac. Sci. Tech. B **8**, 393 (1990).

14. S. Luryi, A. Zaslavsky in *Modern Semiconductor Device Physics*, S. M. Sze, Ed

(Wiley-Interscience, New York, 1998), pp 253-341.

15. A. R. Bennofoi, D. H. Chow, T. C. McGill, Appl. Phys. Lett. **47**, 888 (1985).

16. F. Beltram, F. Capasso, S. Luryi, S. N. G. Chu, A. Y. Cho, Appl. Phys. Lett. **53**, 219 (1988).

17. J. P. Eisenstein, L. N. Pfeiffer, K. W. West, Appl. Phys. Lett. **57**, 2324 (1990).

18. K. M.Brown et al., Appl. Phys. Lett. **64**, 1827 (1994).

19. M. V. Weckwerth et al., Superlattices and Microstructures **20**, 561 (1996).

20. J. A. Simmons et al., J. Appl. Phys. **84**, 5626 (1998).

21. M. A. Blount et al., Semiconductor Science and Technology **13**, A86 (1998).

22. J. S. Moon et al., Electron. Lett. **34**, 921 (1998).

23. J. S. Moon, J. A. Simmons, M. A. Blount, J. L. Reno, M. J. Hafich, Appl. Phys. Lett. **74**, 314 (1999).

24. The issue of whether tunneling through the two barriers is coherent or sequential is similar to that in conventional RTDs. For a discussion, see e.g. S. Luryi, Superlattices and Microstructures **5**, 375 (1989) and references therein.

25. We note that an alternative 3-layer DELTT device structure could allow the electrons to exit vertically from the collector and out the back of the device, rather than laterally. This would lower the effective contact resistance, and allow a smaller lateral device dimension.

26. We note that a second, smaller resonant peak also appears, for $V_{EC} \leq 0.05$ V at 77 K. This is attributed to resonant tunneling from the thermally occupied *second* subband of the emitter into the ground subband of the resonant layer. (At lower temperatures this peak is absent.) The Hartree simulation of Figure 3(a) yields an energy

difference E_{R0}-E_{E1} = 2.44 meV, predicting a V_P for this second peak of 0.025 V, in fair agreement with the data.

27. For the more negative values of V_{TC} there is also apparent a small peak occurring near V_{EC} = 0.39 V, independent of V_{TC}. It is attributed to resonant tunneling in the ungated regions of the device.

28. Preliminary S–parameter measurements indicate that the charging time, like in RTDs, is more closely approximated by $\tau = C_{EC}\sqrt{R_S R_{NDR}}$, where R_{NDR} is the most negative value of the negative differential resistance, and R_s is the 2D channel resistance. See E. R. Brown et al., Appl. Phys. Lett. **58**, 2291 (1991). We note that the transit time delay through the wide collector region is roughly 1 psec and should have a nearly negligible effect on the high-speed performance.

29. For sample EA339, the tunneling resistance is roughly 4 orders of magnitude larger than the in-plane resistance of the 2D lead regions at 77 K, and clearly dominates the measurement of J_P. However, as the thickness of the tunneling barrier is decreased in the other samples, the resistance of the in-plane 2DEG leads begins to play a larger role. Thus our measurements of the PVR and current densities for samples EA492 and EA493 represent lower bounds. We estimate that subtraction of the in-plane 2DEG resistance in sample EA493 would result in a 77 K current density value that is ~50% higher than indicated in Fig. 4.

30. T. Inata et al., Jpn. J. Appl. Phys., **26** L1332 (1987).

31. J. R. Soderstrom et al., Appl. Phys. Lett. **58**, 275 (1991).

32. The authors thank N. E. Harff, S. K. Lyo, and D. C. Tsui for numerous helpful discussions. Sandia is a multiprogram laboratory operated by Sandia Corporation, a

Lockheed Martin company, for the U. S. Dept. of Energy under Contract DE-AC04-94AL85000.

TABLE 1. Device parameters.

L_{EB} is the emitter barrier thickness; L_{CB} is the collector barrier thickness; V_p is the emitter-collector voltage at the main resonance peak in the I-V; PVR is the peak-to-valley current ratio.

Device	L_{EB} (nm)	L_{CB} (nm)	V_p (V)	PVR (77 K)
EA339	12	8	0.36	32:1
EA338	10	8	0.5	20:1
EA491	8	8	0.65	15:1
EA492	7	7	1.4	3:1
EA493	6	6	1.63	1.1:1

Figure Captions

Fig. 1. (a) Typical conduction band profile of the 3-layer DELTT, with an emitter-collector bias applied. The wavefunction separations L_{ER} and L_{EC} are indicated. (b) Schematic diagram of the 3-layer DELTT device structure, showing the 2D emitter and collector layers, the 2D resonant layer, and the control gate. The emitter and collector layers are each selectively contacted via a selective gate depletion technique.

Fig. 2. Emitter-collector current I_{EC} vs. voltage V_{EC} of a single device from the EA339 wafer, measured at 77 K for several values of V_{TC}. The inset shows how the peak voltage V_P changes as a function of control gate voltageV_{TC}.

Fig. 3. (a) Results of an equilibrium self-consistent Hartree calculation of the band structure of 3-layer DELTT EA339. Zero energy represents the Fermi level. Significant free electron densities appear only in the emitter QW and at the far side of the collector. The energies of several subbands are indicated. The difference in energy between the emitter and ground subbands is 28.7 meV. (b) Photoluminescence data from wafer EA339. The difference in energy between the emitter and resonant QW ground subbands is 27.6 meV, close to the value obtained from the Hartree calculation.

Fig. 4. Measured peak current density J_P vs. emitter barrier thickness L_{EB} for the devices in Table 1, which all had emitter densities of ~2.5 x 10^{11}. The solid line is a fit to the data. Extrapolation of the fit to a barrier thickness of 28 Å yields a current density of 8.2

x 10^3 A/cm2, comparable to the higher values seen in RTDs. The dashed line represents the expected J_p for the case of an emitter QW with an electron density of $1x10^{12}/cm^2$.

Fig. 5. (a) Emitter-collector I-V characteristics of 3-layer DELTT EA339 at $V_{TC} = 0$ and several different temperatures. A strong negative differential resistance persists to 250 K. The PVR decreases at higher temperatures, primarily due to an increase in valley current. (b) Emitter-collector I-V characteristics of 3-layer DELTT EA338 at 273 K (0 °C) at several different gate voltages V_{TC}. Clear gate-control of the NDR is apparent, close to room temperature.

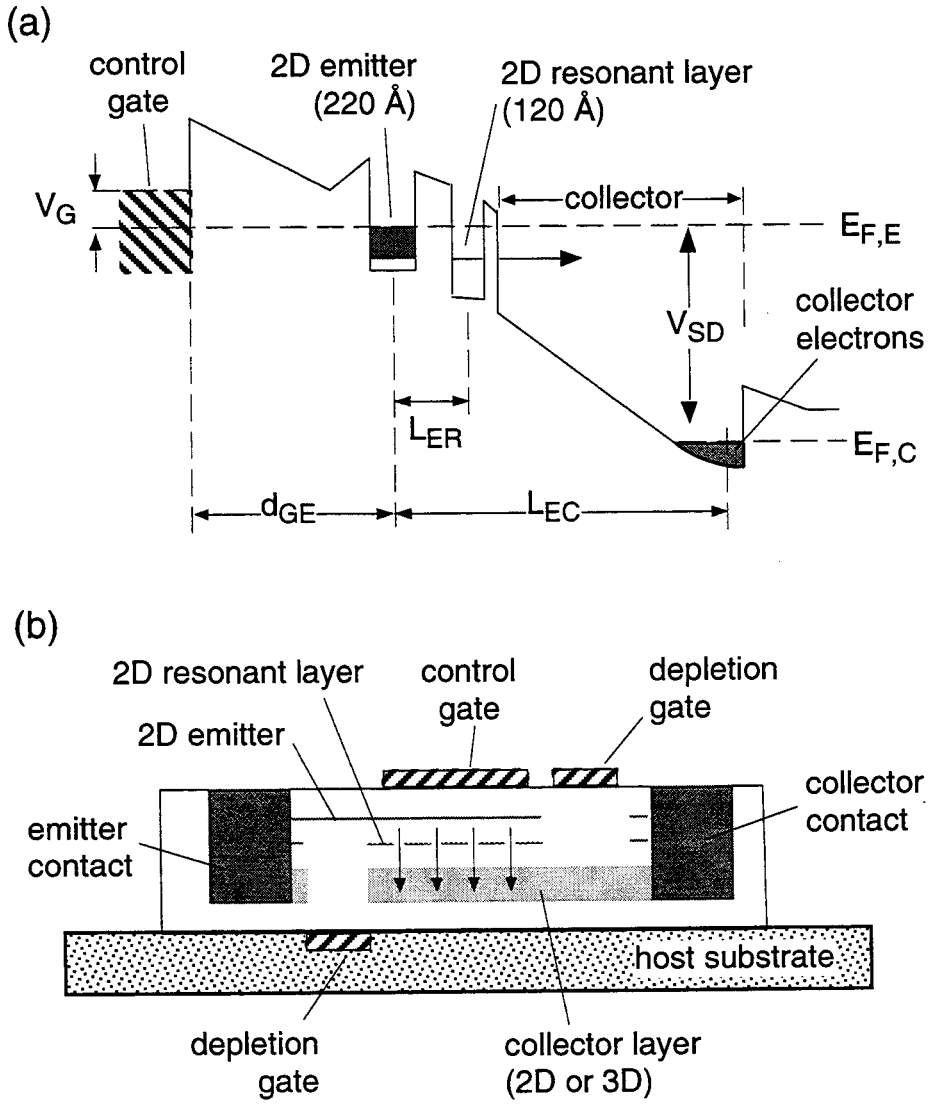
(a)
control gate
2D emitter (220 Å)
2D resonant layer (120 Å)
collector
V_G
$E_{F,E}$
V_{SD}
collector electrons
L_{ER}
$E_{F,C}$
d_{GE}
L_{EC}
(b)
2D resonant layer
control gate
depletion gate
2D emitter
collector contact
emitter contact
host substrate
depletion gate
collector layer (2D or 3D)

Fig. 1

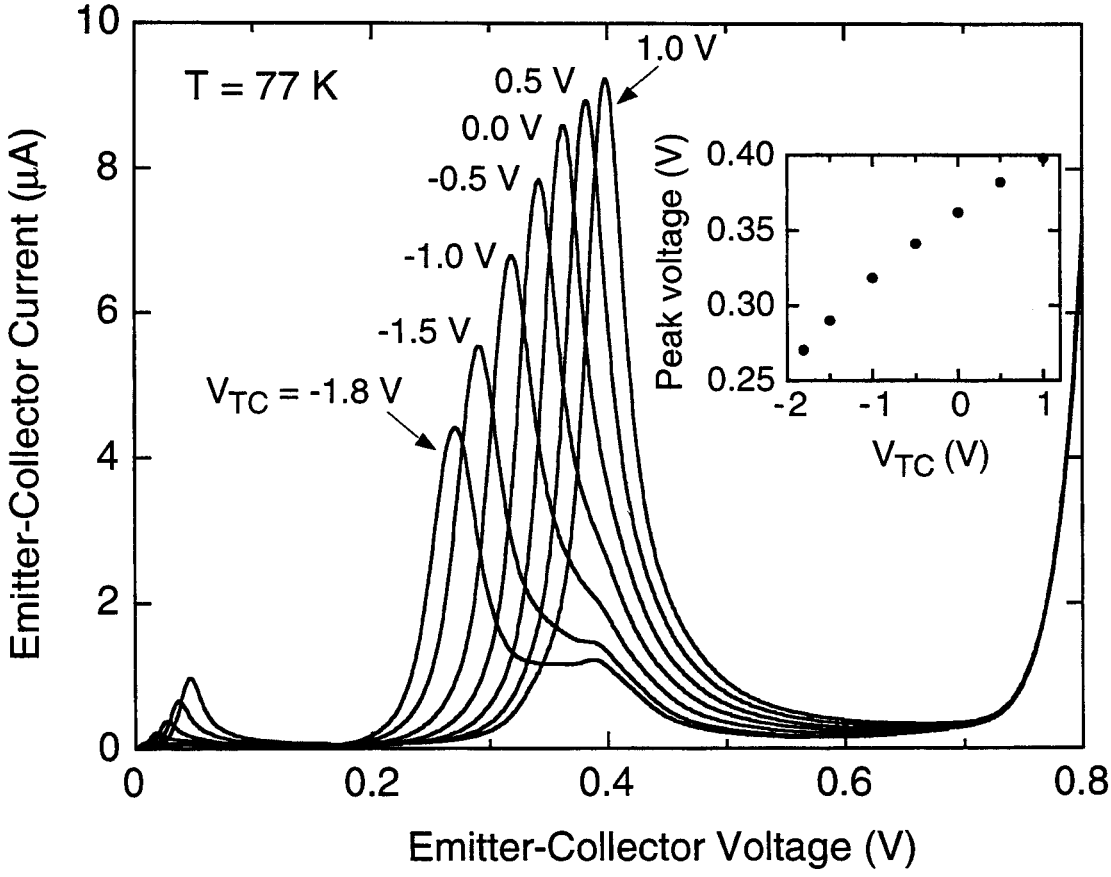
T = 77 K
1.0 V
0.5 V
0.0 V
-0.5 V
-1.0 V
-1.5 V
V_{TC} = -1.8 V
Emitter-Collector Current (μA)
Emitter-Collector Voltage (V)
Peak voltage (V)
V_{TC} (V)

Fig. 2

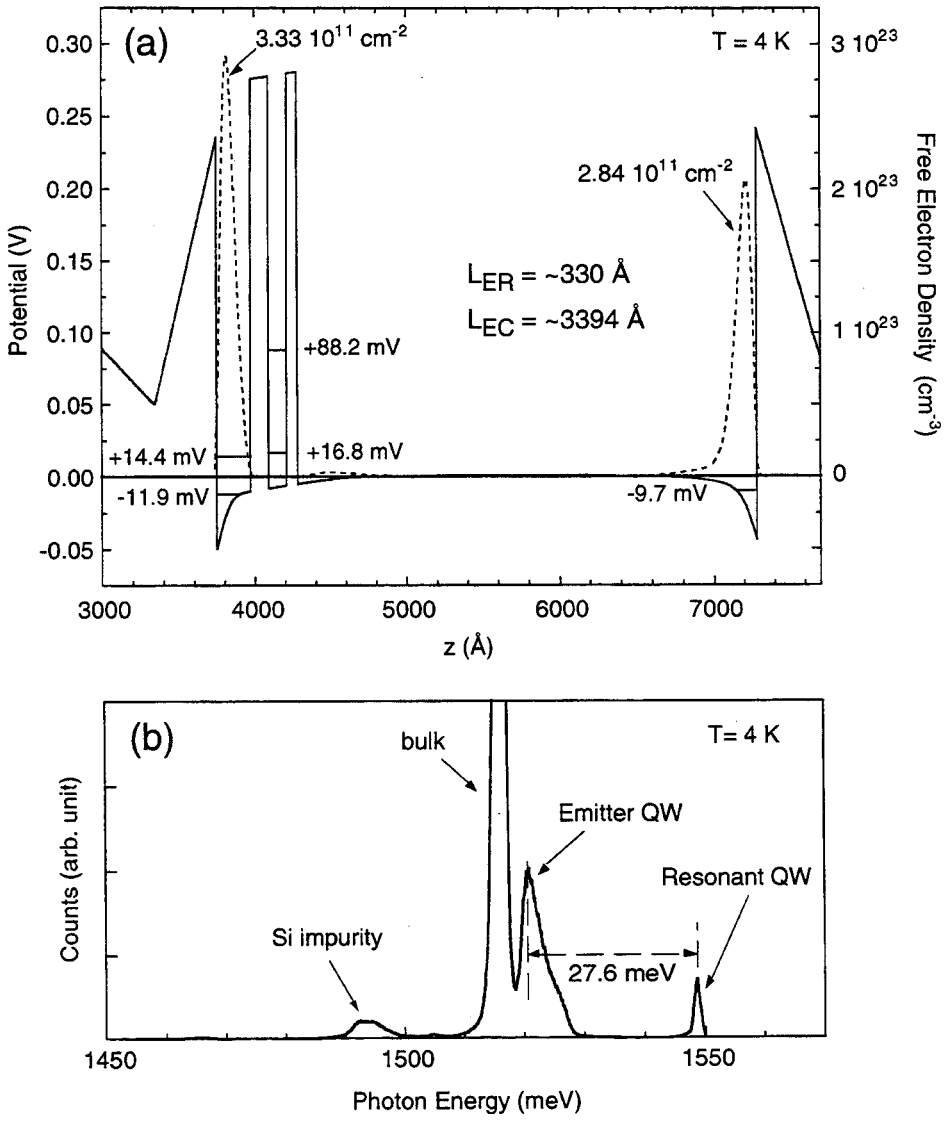
(a)
3.33 10^11 cm^-2
T = 4 K
2.84 10^11 cm^-2
L_ER = ~330 Å
L_EC = ~3394 Å
+88.2 mV
+14.4 mV
+16.8 mV
-11.9 mV
-9.7 mV
Potential (V)
Free Electron Density (cm^-3)
z (Å)
(b)
bulk
T= 4 K
Emitter QW
Resonant QW
Si impurity
27.6 meV
Counts (arb. unit)
Photon Energy (meV)

Fig. 3

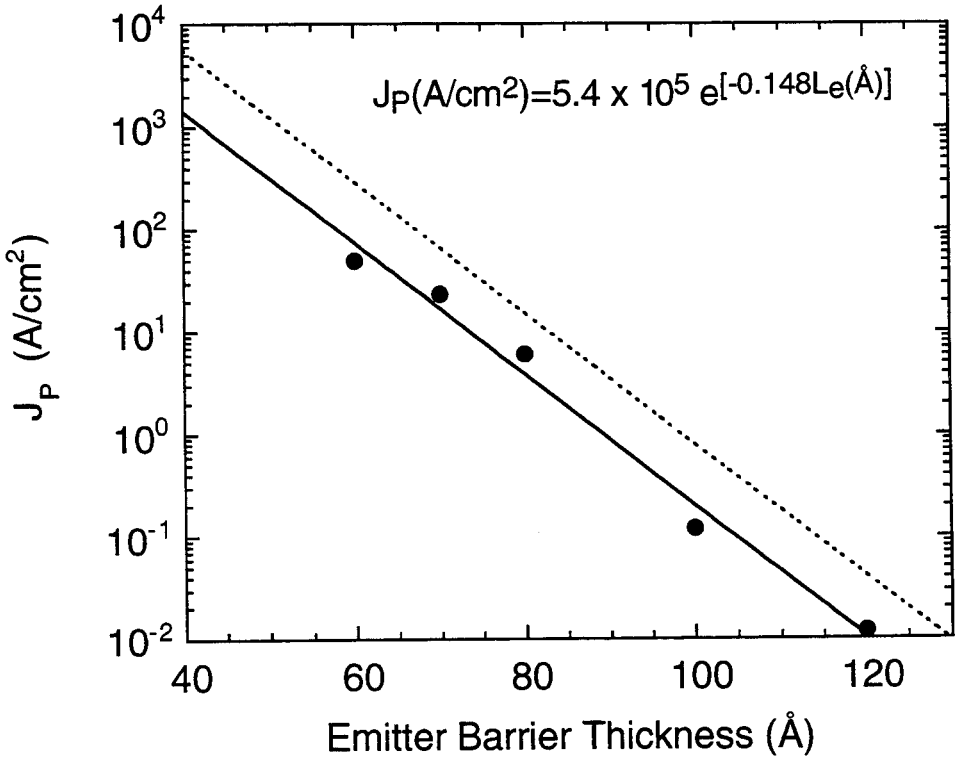
$J_P(A/cm^2)=5.4 \times 10^5 e^{[-0.148Le(Å)]}$
J_P (A/cm^2)
10^4
10^3
10^2
10^1
10^0
10^{-1}
10^{-2}
40
60
80
100
120
Emitter Barrier Thickness (Å)

Fig. 4

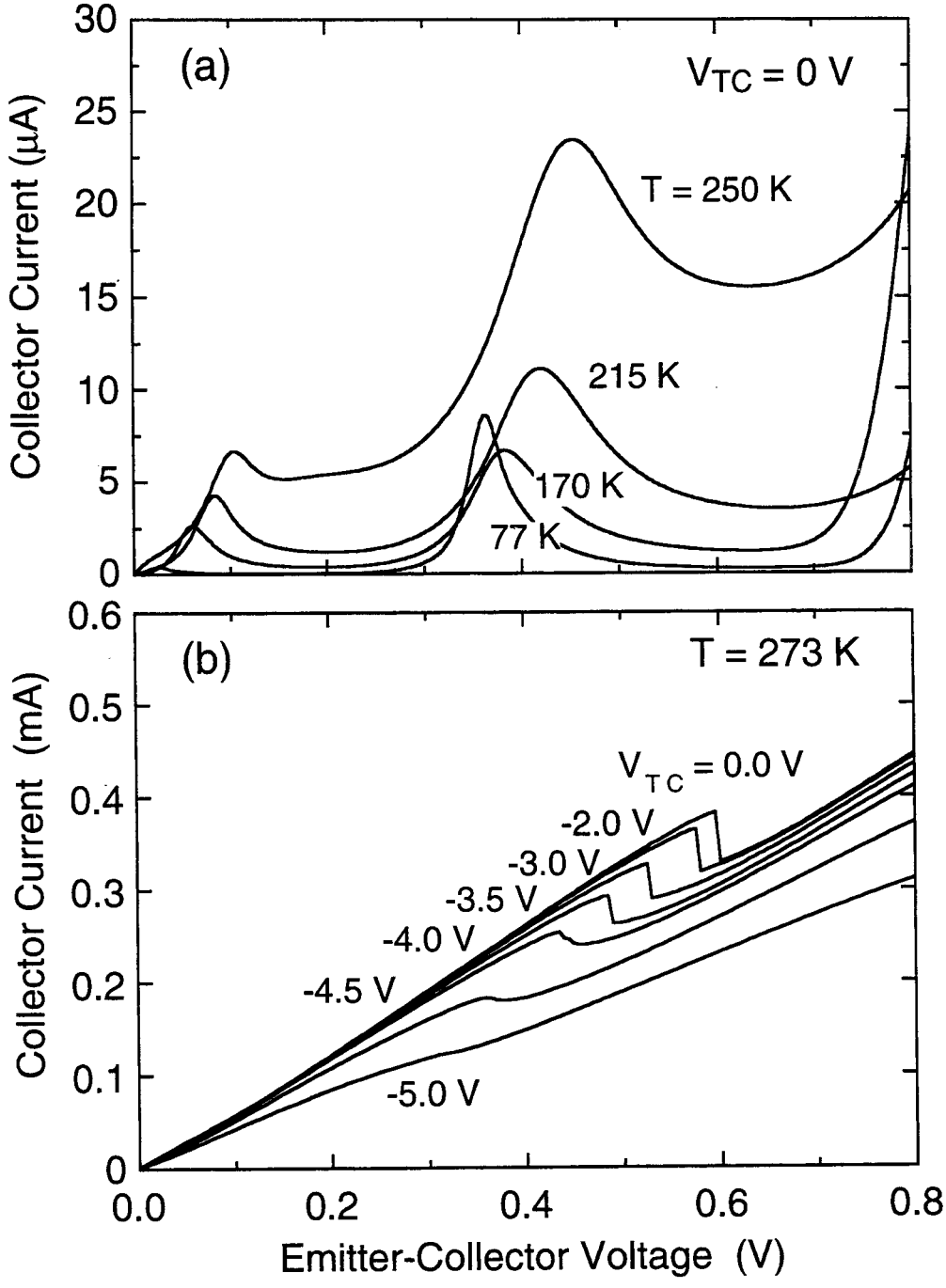
(a)
V_{TC} = 0 V
T = 250 K
215 K
170 K
77 K
Collector Current (μA)
30
25
20
15
10
5
0
(b)
T = 273 K
V_{TC} = 0.0 V
-2.0 V
-3.0 V
-3.5 V
-4.0 V
-4.5 V
-5.0 V
Collector Current (mA)
0.6
0.5
0.4
0.3
0.2
0.1
0
0.0
0.2
0.4
0.6
0.8
Emitter-Collector Voltage (V)

Fig. 5

Appendix III. "Non-Equilibrium DC and Photon-Assisted Interlayer Tunneling in a Bi-Layer Tunneling Structure"

ELSEVIER

Physica B 314 (2002) 417–421

PHYSICA B

www.elsevier.com/locate/physb

Nonequilibrium DC and photon-assisted interlayer tunneling in a bi-layer tunneling structure

S.K. Lyo*, J.A. Simmons

Sandia National Laboratories, Albuquerque, NM 87185, USA

Abstract

We study nonequilibrium DC and photon-assisted tunneling (PAT) of electrons between two weakly tunnel-coupled biased electron layers. The PAT current is related to the DC current. The line shape of the PAT current is studied as a function of the bias energy and the temperature. The contributions from the intrinsic screened electron–phonon and electron–electron scattering to the widths of the tunneling spectra are examined. Calculated DC tunneling current is compared with recent data. © 2002 Elsevier Science B.V. All rights reserved.

PACS: 73.40.Kp; 73.63.Hs; 78.67.De

Keywords: Tunneling; Photon; Quantum wells; Nonequilibrium

1. Introduction

Tunneling of electrons under the influence of intense low-energy photons in layered semiconductors is a subject of current interest [1–6]. In the tunneling structures studied in the past, electrons flow in from the three-dimensional (3D) source region along the growth (i.e., z) direction, tunnel through a multi-barrier structure, and flow out in the z direction to the sink. Parts of the structure are under the radiation in various studies. We are interested in a different tunneling structure: the current flows in laterally through the top GaAs quantum well (QW1), tunnels through the wide $Al_xGa_{1-x}As$ barrier and flows out of the bottom QW (QW2) laterally. The chemical potentials μ_1 and μ_2 of QW1 and QW2 are shifted relative to each other by the bias energy $V_{DQW} = \mu_2 - \mu_1$. The two QWs are in equilibrium separately. This structure was fabricated recently for 2D–2D tunneling transistors [7]. A formalism for nonlinear DC tunneling was given earlier [8]. For photon-assisted tunneling (PAT), QW2 is under an intense and uniform oscillating sinusoidal potential energy $U_2(t) = E_{AC}\cos(\omega t)$ relative to QW1, neglecting the in-plane resistance compared with the tunneling resistance. This model was used by Tien and Gordon to study the effect of intense microwave radiation on tunneling between superconducting films [9].

In this paper, we study the contributions from the intra-QW electron–electron, electron–impurity, and electron–phonon scattering to the line shape of the DC and PAT current as a function of the temperature (T), using a random phase approximation for screening [8]. For the

*Corresponding author. Tel.: +1-505-844-3718; fax: +1-505-844-1197.

E-mail address: sklyo@sandia.gov (S.K. Lyo).

PII: S0921-4526(01)01429-6

electron–phonon scattering, deformation potential, piezoelectric interactions, and LO-phonon scattering are considered. Sharp resonances are found for the current due to energy and momentum conservation in the restricted 2D phase space even at high temperatures. The resonance energy for the tunneling current can be controlled by V_{DQW}.

2. Photon-assisted tunneling

We calculate the tunneling rate of an electron from an initial state $|1s\rangle$ in QW1 to a final state $|2k\rangle$ in QW2 to the lowest order in the tunneling integral $t_{2k,1s} = \langle 2k|H|1s\rangle$ by expanding the time-dependent wave function in terms of the tunnel-free eigenstates:

$$\psi(t) = \sum_k c_{1k}(t)e^{-i\varepsilon_{1k}t/\hbar}\psi_{1k} + \sum_k c_{2k}(t)e^{-i\varepsilon_{2k}t/\hbar}\psi_{2k}e^{-i\alpha\sin(\omega t)}. \quad (1)$$

Here, ε_{jk} is the energy of ψ_{jk}, $c_{1k}(0) = \delta_{k,s}$, $c_{2k}(0) = 0$, and $\alpha = E_{ac}/\hbar\omega$. The rate is given by

$$W_{1\to 2} = \sum_k \frac{d}{dt}|c_{2k}(t)|^2 = \frac{2\pi}{\hbar}\sum_{n,n'=-\infty}^{\infty} J_n(\alpha)J_{n'}(\alpha)\cos[(n-n')\omega t] \times (2-\delta_{n,n'})\sum_k |t_{2k,1s}|^2\delta(\varepsilon_{2k}-\varepsilon_{1s}+n\hbar\omega), \quad (2)$$

where $J_n(\alpha)$ is the nth order Bessel function and n the integers. The contributions from $n = n'$ and $n \neq n'$ in Eq. (2) yield DC and AC PAT current, respectively.

Eq. (2) is generalized to include the effect of the interactions. We introduce a tunneling operator $\hat{t} = \sum t_{2k',1k}a^{\dagger}_{2k'}a_{1k} + \text{h.c.}$, where $a^{\dagger}_{jk}$ and a_{jk} are Fermion creation and destruction operators and replace ε_{jk} by $\varepsilon_{jk} - \mu_j$. Here, μ_j is the chemical potential. We now replace the noninteracting states labels jk by those of the exact eigenstates of the interacting Hamiltonian, multiply by the thermodynamic weighting factor, and subtract the back current, obtaining [8]

$$I_{tun} = \frac{4e}{\hbar}\sum_{n,n'=-\infty}^{\infty} J_n(\alpha)J_{n'}(\alpha) \times \cos[(n-n')\omega t](2-\delta_{n,n'})\sigma(\Omega_n) \quad (3a)$$

$$\sigma(\Omega_n) = \text{Im}\, F(\omega_r \to \Omega_n + i0), \quad (3b)$$

$$F(\omega_r) = \int_0^{\beta} e^{\omega_r u}\langle e^{uH}\hat{t}e^{-uH}\hat{t}\rangle\, du,$$

where H is the full Hamiltonian without $\hat{t}$. $\Omega_n = \mu_1 - \mu_2 + n\hbar\omega$, $\beta = (k_B T)^{-1}$, $\omega_r = 2\pi i r\beta^{-1}$ is on the imaginary axis and r is an integer. In Eq. (3a), e is the electronic charge and ω_r is analytically continued to slightly above the real axis in the complex plane. The spin degeneracy is included. The expression in Eq. (3b) has the same form as Kubo's current correlation function for the conductivity. In the absence of the radiation (i.e., for $\alpha = 0$), Eq. (3) reduces to the result obtained earlier for the nonequilibrium tunneling current except for the sign change in the definition of the DC bias V_{DQW} [8]. Although the result in Eq. (3) is valid for inter-sublevel tunneling, our application is mainly for tunneling between the ground sublevels.

We study the DC part (i.e., $n = n'$) of the current in Eq. (3) given by

$$I_{tun,DC} = \frac{4e}{\hbar}\sum_n J_n(\alpha)^2\sigma(\Omega_n), \quad (4)$$

where $\Omega_n = n\hbar\omega - V_{DQW}$. Basic features of $\sigma(\Omega)$ were recently studied for $\omega = 0$ in the absence of the oscillating field (i.e., for $\alpha = n = 0$ in Eq. (4)) [8]. The function $\sigma(\Omega)$ is peaked near $\Omega = \Delta_0$ where Δ_0 is the energy separation of the sublevel of QW2 relative to that of QW1 for $V_{DQW} = 0$. This means that maximum tunneling current occurs when the energy-dispersion curves of the two QWs are aligned by a negative bias $V_{DQW} = -\Delta_0$ in the absence of the oscillating field. When the radiation field is applied, the net photon energy for the peak current equals the energy difference between the two dispersion curves (i.e., $n\hbar\omega \approx V_{DQW} + \Delta_0$). The resonance photon energy can therefore be tuned by V_{DQW}.

3. Numerical evaluation

We calculate the DC and PAT current using the methods described in Ref. [8] and Section 2 and the effective mass approximation with $m^* = 0.067m_0$ in the QWs (m_0 is the free electron mass). In Fig. 1, we compare, at 77 K, the calculated DC tunneling current with the data from 120–125–120 Å $GaAs/Al_{0.3}Ga_{0.7}As$ double QWs with 2D electron densities $N_1 = 8 \times 10^{11}$ and $N_2 = 2 \times 10^{11}\,cm^{-2}$ and the area 0.02 cm × 0.05 cm. The peak occurs near the Fermi energy difference $V_{DQW} = \mu_1 - \mu_2 = 28.7 - 7.2 = 21.5$ meV, when the two bands align. We have employed $t_{12} = 10^{-3}$ meV, which is a reasonable value for the structure. Other standard parameters are given in Ref. [8]. We employ adjustable parameters $\Gamma_1 = 12$ meV and $\Gamma_2 = 4$ meV for the energy-level damping from the static impurities to fit the data. Here, the ratio Γ_2/Γ_1 is chosen to equal the ratio of the observed mobilities in QW1 and QW2. The contribution from acoustic phonon scattering is not shown in Fig. 1(a) because it is very small. The rise in current arounf $V_{SD} = 55$ mV in Fig. 1(b) is due to the leakage in the control gate [7]. Note that V_{DQW} in Fig. 1(a) is the voltage drop between QW1 and QW2, while V_{SD} in Fig. 1(b) is the source–drain voltage which includes the voltage drop in the QW planes. The in-plane resistance skews the I–V curve in Fig. 1(a) to the right as in Fig. 1(b).

The calculated intrinsic I–V curve becomes much sharper in the absence of impurity scattering (i.e., $\Gamma_1 = \Gamma_2 = 0$) as shown in Fig. 2 at 77 K for the same parameters. At 300 K, however, the curve becomes significantly broadened. The second peak at 300 K is from tunneling into the empty second sublevel in QW2 for the same value of t_{12}. It is interesting to note that the contribution from electron–electron scattering is much more important than that from LO-phonon scattering at $77\,K \ll \hbar\omega_{LO}/k_B = 36.5\,meV/k_B$ and is comparable with the latter at 300 K in this high-density system. In the electron–electron scattering process, electrons in QW1 relax their energy by scattering other electrons out of the Fermi sea before tunneling into QW2. The electron–electron contribution decreases with decreasing electron density.

Fig. 3 shows the calculated intrinsic PAT current at 77 and 300 K for $E_{AC} = 10$ meV. The one-, two-, and three-photon contributions are clearly resolved with peaks at $\hbar\omega = 21.3$, 10.7, and 7.4 meV at 77 K. The relative contributions from various scattering mechanisms are similar to those

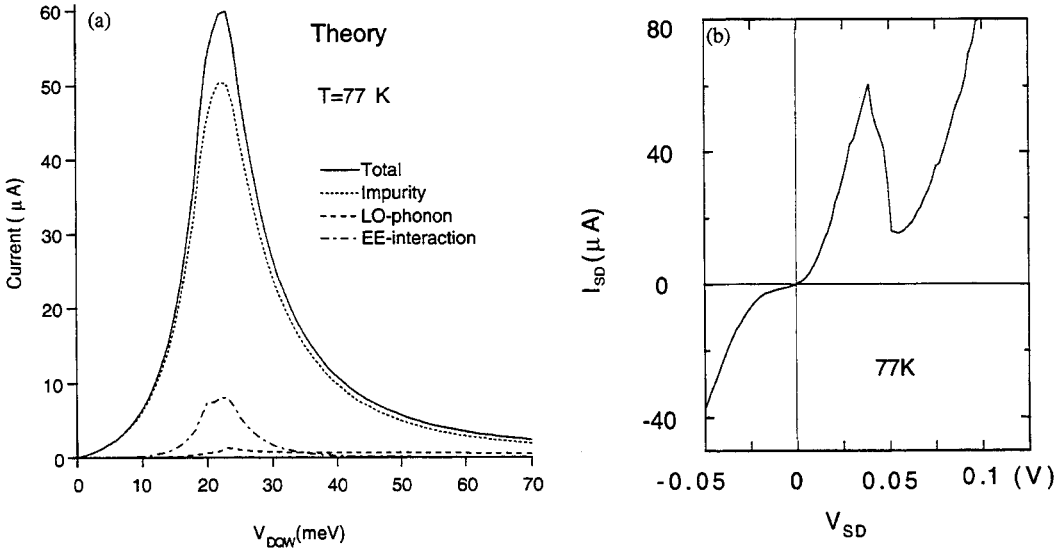

Fig. 1. Comparison of the (a) calculated DC tunneling current with (b) data at 77 K. The quantity V_{DQW} (V_{SD}) is the bias energy between the QWs (the source drain voltage).

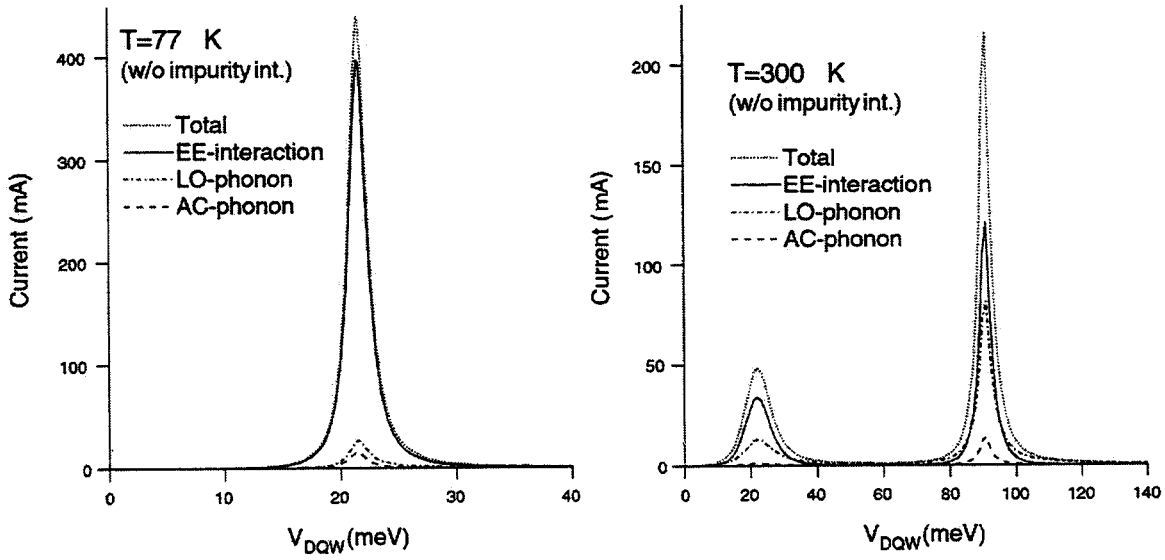

Fig. 2. Comparison of various scattering contributions to the intrinsic DC tunneling current at 77 and 300 K.

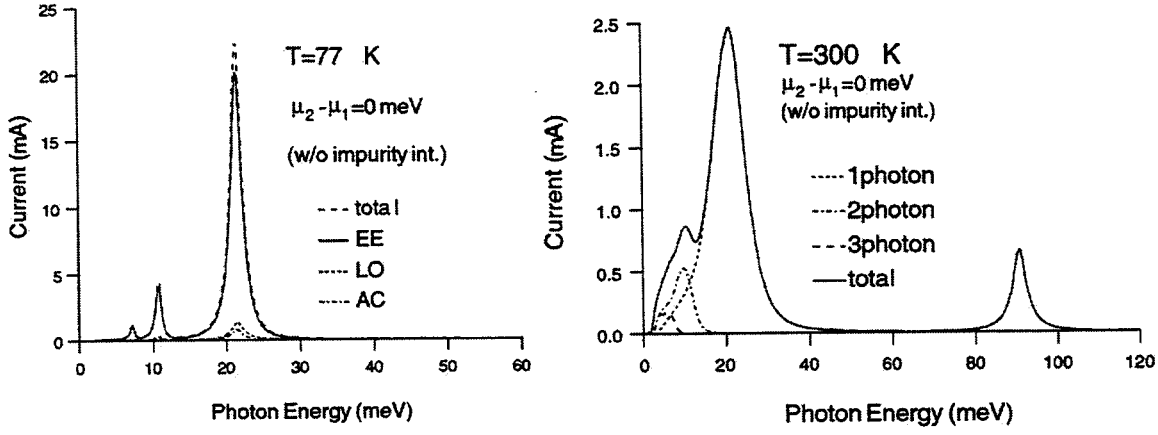

Fig. 3. Spectra for the intrinsic photon-assisted current at 77 and 300 K.

in Fig. 2. The n-photon peaks broaden considerably and overlap at 300 K. The PAT current into the second empty sublevel in QW2 is smaller because of a smaller value of $\alpha = E_{AC}/\hbar\omega$. The PAT current peaks move up (down) in energy for increasing (decreasing) V_{SD}.

4. Summary

In summary, we have studied the line shape of the nonequilibrium DC and PAT current between two weakly tunnel-coupled electron layers as a function of the DC bias energy and the temperature. The contributions from the intrinsic screened electron–phonon and electron–electron scattering to the widths of the tunneling spectra were examined.

Acknowledgements

Sandia is a multiprogram laboratory operated by Sandia corporation, a Lockheed Martin

Company, for the US DOE under Contract No. DE-AC04-94AL85000.

References

[1] B.J. Keay, et al., Phys. Rev. Lett. 75 (1995) 4098.
[2] H. Drexler, et al., Appl. Phys. Lett. 67 (1995) 2816.
[3] P. Johansson, Phys. Bev. B 41 (1990) 9892.
[4] J. Inărrea, G. Platero, C. Tejedor, Phys. Rev. B 50 (1994) 4581.
[5] C.A. Stafford, N.S. Wingreen, Phys. Rev. Lett. 76 (1996) 1916.
[6] S.K. Lyo, Phys. Rev. B 64 (2001) 113311, and references therein.
[7] J.A. Simmons, et al., J. Appl. Phys. 84 (1998) 5626.
[8] S.K. Lyo, Phys. Rev. B 61 (2000) 8316.
[9] P.K. Tien, J.P. Gordon, Phys. Rev. 129 (1963) 647.

Appendix IV. "Photon-Assisted Transmission Through a Double-Barrier Structure"

PHYSICAL REVIEW B, VOLUME 64, 113311

Photon-assisted transmission through a double-barrier structure

S. K. Lyo
Sandia National Laboratories, Albuquerque, New Mexico 87185
(Received 12 December 2000; published 31 August 2001)

We study multiphoton-assisted transmission of electrons through single-step, single-barrier and double-barrier potential-energy structures as a function of the photon energy and the temperature. Sharp resonances are obtained for the spectra of the tunneling current and are relevant to infrared detectors.

DOI: 10.1103/PhysRevB.64.113311 PACS number(s): 78.90.+t, 78.66.Fd, 73.40.Gk

I. INTRODUCTION

Transport of electrons under the influence of intense low-energy photons in artificially structured semiconductors has received increasing attention recently. Experimentally, photon-assisted tunneling has been observed for resonant tunneling through a single quantum well,[1] quantum dots,[2] and multi-quantum wells and superlattices.[3,4] Theoretically, Tien and Gordon[5] studied the effect of microwave radiation on superconducting tunneling devices. Subsequent theoretical studies have investigated the effect of different forms of ac modulation of the potentials for various structures using different approaches.[6–11] These studies include double-barrier photon-assisted tunneling through a resonant level with a finite lifetime using a tunneling-Hamiltonian approach under a local ac modulation of the tunneling structure,[6] investigation of a similar structure when the whole structure is modulated by a propagating microwave radiation,[7] and photon-assisted tunneling through a double quantum-dot system.[8] Many-body effect for double-barrier photon-assisted tunneling has also been studied recently.[9] In this paper, we study photon-assisted transmission of electrons through yet new structures such as single-step and single-barrier structures as well as multibarrier (e.g., double-barrier) structures as a function of the photon energy and the temperature in two and three dimensions using a boundary-matching method[10] and Tien-Gordon ac modulation model.[5] Sharp resonances are found in the tunneling current through double-barrier structures and may have valuable applications for IR (infrared) detectors.

II. PHOTON-ASSISTED TUNNELING AND ACTIVATION

We study the transmission of an electron through a general double-barrier structure shown in the inset of Fig. 1. The structure reduces to a single-step barrier for the special case $V_2=V_3=V_4=V_5$ and to a single barrier for $V_2>V_3=V_4=V_5$. The electron has an effective mass m_i^* in the regions $i=1,\ldots,5$. Region 1 is in contact with the source and is under a highly conducting metallic gate that drives the electron with an intense and uniform oscillating sinusoidal potential energy $V_1=\varepsilon_{ac}\cos(\omega t)$.[5] Region 5 is in contact with the drain.

The time-dependent wave function of an incoming electron with a wave number k reflected at the boundary at $x_1=0$ is given, in region 1 ($x<0$, inset of Fig. 1), by

$$\psi_1=A_{1k}^{+}\exp[i(kx-\omega_k t)]\exp[-i\alpha\sin(\omega t)]+\sum_{k'}A_{1k'}^{-}\exp[i(k'x-\omega_{k'}t)]\exp[-i\alpha\sin(\omega t)], \tag{1}$$

where $\hbar\omega_k=(\hbar k)^2/2m_1^*$ and $\alpha=\varepsilon_{ac}/\hbar\omega$. The factor $\exp[-i\alpha\sin(\omega t)]$ in Eq. (1) accounts for the time-dependent V_1 in the Hamiltonian and can be expanded into the Fourier components $\exp[-i\alpha\sin(\omega t)]=\Sigma J_n(\alpha)\exp(in\omega t)$, where $J_n(\alpha)$ is the nth order Bessel function and n runs over the integers. Matching the boundary conditions at $x=x_1$ requires the reflected wave k' to take only the discrete values that generate the same time-Fourier components as the incoming waves, yielding

$$\psi_1=A_{1k}^{+}e^{ikx}\sum_{n=-\infty}^{\infty}J_n(\alpha)\exp[-i(\omega_k+n\omega)t]+\sum_{n,n'=-\infty}^{\infty}A_{1k_{1,n-n'}}^{-}\exp[-ik_{1,n-n'}x]J_{n'}(\alpha)\times\exp[-i(\omega_k+n\omega)t], \tag{2}$$

where $k_{1,n}=[2m_1^*(\omega_k+n\omega)/\hbar]^{1/2}$. This quantity as well as other $k_{j,n}$ to be defined later is assumed to take positive imaginary values when the argument inside the brackets becomes negative.

In the regions $j=2,\ldots,5$, the wave functions are linear superpositions of free plane-wave states without the time-dependent part $\exp[-i\alpha\sin(\omega t)]$. Taking only the same time-Fourier components as the incoming waves, we write

$$\psi_j=\sum_n A_{jk_{j,n}}^{\mp}e^{\pm ik_{j,n}x}\exp[-i(\omega_k+n\omega)t]\quad(j=2,\ldots,5), \tag{3}$$

where $k_{j,n}=[2m_j^*(\omega_k+n\omega-V_j/\hbar)/\hbar]^{1/2}$ and $A_{5k_{5,n}}^{-}=0$. The A coefficients satisfy the boundary conditions for the continuity of the wave function and the current density at the boundaries x_j for all t, yielding for $j=2$, 3, and 4

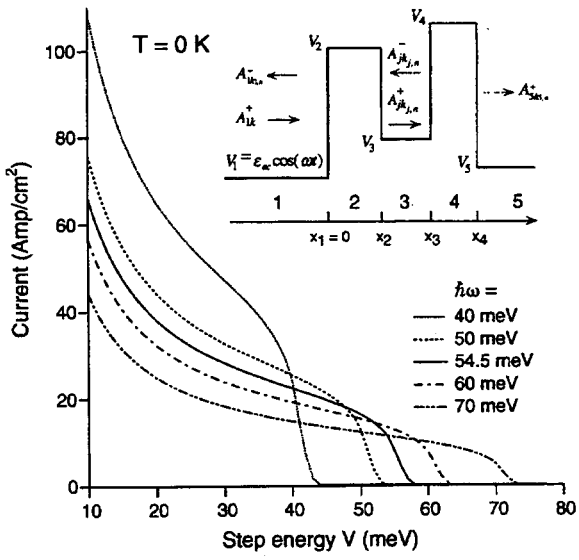

FIG. 1. Photon-assisted current density through a single potential step with energy $V(=V_2=\cdots=V_5)$ in three dimensions at 0 K. The inset shows a double-barrier structure. The A coefficients denote the amplitude of the nth time-Fourier component of the left- and right-going waves. Region 1 is driven by an intense sinusoidal potential energy $V_1(t)$.

$$A^{\pm}_{jk_{j,n}} = \frac{1}{2\gamma_j k_{j,n}}[(\gamma_j k_{j,n} \pm \gamma_{j+1}k_{j+1,n}) \times \exp(ik_{j+1,n}x_j)A^{+}_{j+1k_{j+1,n}} + (\gamma_j k_{j,n} \mp \gamma_{j+1}k_{j+1,n}) \times \exp(-ik_{j+1,n}x_j)A^{-}_{j+1k_{j+1,n}}]e^{\mp ik_{j,n}x_j}, \quad (4)$$

where $\gamma_j = 1/m_j^*$ and the second term is zero for $j=4$ (i.e., $A^{-}_{5k_{5,n}}=0$). The relationship in Eq. (4) is valid for a *multibarrier structure* in general. Employing the recurrence relationship in Eq. (4) repeatedly, the A coefficients are determined in terms of $A^{+}_{5k_{5,n}}$ in the regions $j=2$, 3, and 4. We therefore define for $j=2$,

$$A^{\pm}_{2k_{2,n}} = P^{\pm}(n)A^{+}_{5k_{5,n}}/(2\gamma_2 k_{2,n}). \quad (5)$$

Here, $P^{\pm}(n)$ is found by successive substitutions of the relationship in Eq. (4).

The boundary conditions at $x_1=0$, yield

$$A^{+}_{1k}J_n(\alpha) + \sum_{n'} A^{-}_{1k_{1,n-n'}}J_{n'}(\alpha) = A^{+}_{2k_{2,n}} + A^{-}_{2k_{2,n}},$$

$$\gamma_1 k\left[A^{+}_{1k}J_n(\alpha) - \sum_{n'} A^{-}_{1k_{1,n-n'}}J_{n'}(\alpha)\right] = \gamma_2 k_{2,n}(A^{+}_{2k_{2,n}} - A^{-}_{2k_{2,n}}). \quad (6)$$

Choosing $A^{+}_{1k}=1$ and inserting Eq. (5) in Eq. (6), the coefficients $A^{-}_{1k_{1,n}} \equiv R_{n,0}$ are given by the following linear equation for the column matrix R:

$$[\{(P^{+}+P^{-})JK_1 + K_2(P^{+}-P^{-})J\}R]_{n,0} = [\{\gamma_1 k(P^{-}+P^{+}) + (P^{-}-P^{+})K_2\}J]_{n,0}, \quad (7)$$

where the matrices $P^{\pm}$, J, and K_j are defined by

$$P^{\pm}{}_{n,n'} = \delta_{n,n'}P^{\pm}(n), \quad J_{n,n'} = J_{n-n'}(\alpha),$$
$$(K_j)_{n,n'} = \gamma_j k_{j,n}\delta_{n,n'}. \quad (8)$$

The reflection coefficients in region 1, $R_{n,0} \equiv A^{-}_{1k_{1,n}}$ are obtained from Eq. (7) by employing a sufficiently large size for the matrices $P^{\pm}$, J, and K_j. The coefficients $A^{\pm}_{2k_{2,n}}$ are obtained from Eq. (6) after inserting these results on the left-hand sides. The transmission coefficients $A^{+}_{5k_{5,n}}$ are then found from Eq. (5).

The transmitted current is given by summing over the contributions from all incoming electrons in region 1. The current per length [two-dimensional (2D)] or area (3D) is given by

$$I_{2,3D} = \frac{em_1^{*2}}{2\pi^2\hbar^2 m_5^*}\int_0^{\infty}\sum_n d\varepsilon_k \frac{k_{5,n}}{k}\left|\frac{A^{+}_{5,k_{5,n}}}{A^{+}_{1k}}\right|^2 F_{2,3D}(\varepsilon_k) \times \theta(n\hbar\omega + \varepsilon_k - V_5),$$

$$F_{3D}(\varepsilon_k) = \frac{k_B T}{\hbar}\ln[e^{-\beta(\varepsilon_k-\mu)}+1],$$

$$F_{2D}(\varepsilon_k) = 2\sqrt{\frac{2k_B T}{m_1^*}}\int_0^{\infty}\frac{dx}{\exp[x^2+\beta(\varepsilon_k-\mu)]+1}, \quad (9)$$

where $\theta(\varepsilon)$ is the unit step function, μ is the chemical potential, $\beta = 1/k_B T$, and T is the temperature. We consider the (nonequilibrium) situation where only region 1 is populated. The electrons in region 5 flow out quickly into the drain.

The photon-assisted current density through a single potential step of energy V is shown in Fig. 1 for a three-dimensional structure at $T=0$ K as a function of V for $\hbar\omega = 40-70$ meV. The electron density is $n = 2\times10^{16}$ cm^3 with the Fermi energy $\varepsilon_F = 4.0$ meV for $m_i^* = 0.067m_0$. We assume a significantly large amplitude $\varepsilon_{ac} = 10$ meV for $V_1(t)$ throughout this paper. The current vanishes when V exceeds the threshold value $\varepsilon_F + \hbar\omega$.

A semilog graph of the current density is shown for the same structure and a 150-Å barrier with the same density in Fig. 2 as a function of the inverse temperature for zero photon intensity (i.e., $\varepsilon_{ac}=0$: solid curve), for $\hbar\omega = 10$ (dashed curve) and 20 meV (dotted curve). The reduction of the activation energy for increasing ω is clearly seen in Fig. 2. For comparison, the dash-dotted curve shows the current through a 150-Å, 50-meV barrier in the absence of the photon field.

The transmission-current spectra are displayed in Fig. 3(a) for the same systems. The main peaks there correspond to transmission through one-photon-assisted activation. A weak two-photon peak is visible near $\hbar\omega = 25$ meV at $T=0$ K for the step potential. The current decays above the peaks because the effective coupling strength α decreases as a function of ω. The current is finite even at $T=0$ K for the barrier

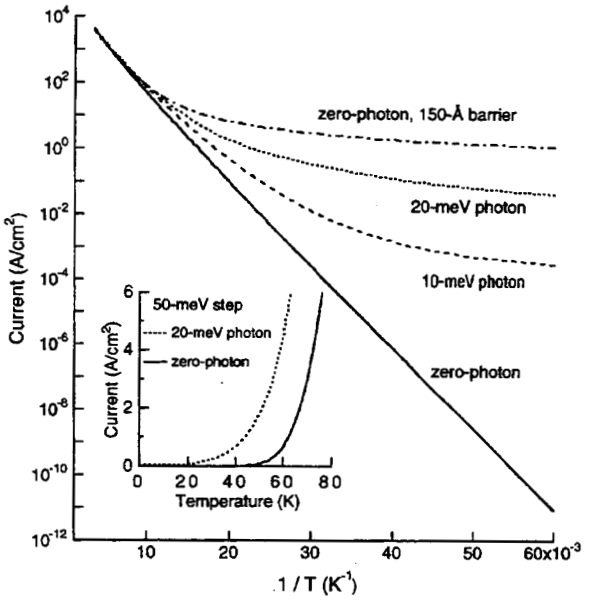

FIG. 2. Transmission current through a 50-meV potential step with zero photon (solid curve), 10-meV (dashed curve) and 20-meV (dotted curve) photons as a function of the inverse temperature. The dash-dotted curve represents a zero-photon thermionic current through a 150-Å, 50-meV barrier. The inset shows a reduction of the threshold temperature caused by 20-meV photons.

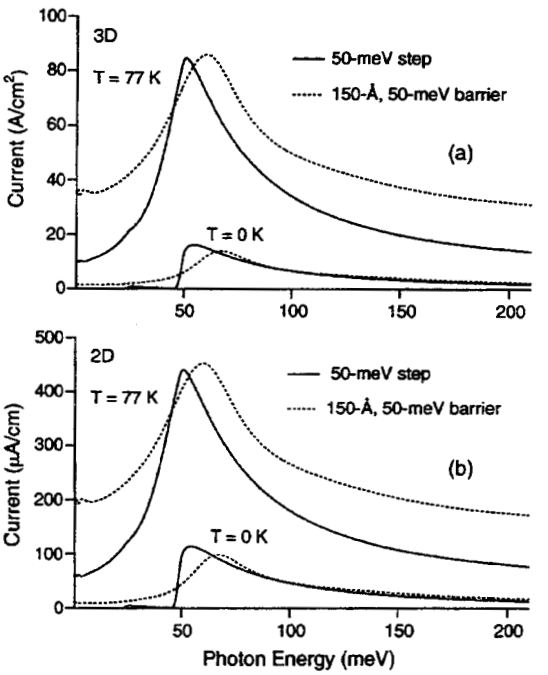

FIG. 3. Transmission-current spectra of the potential-step and the barrier structures studied in Fig. 2 at 0 K and 77 K in (a) three and (b) two dimensions.

potential as expected. The one-photon current peaks at $\hbar\omega = 54.5$ meV for the step at 0 K. This is also seen in Fig. 1 at $V = 50$ meV, where the solid curve is above all other curves. Similar but somewhat sharper spectra are obtained in Fig. 3(b) for a two-dimensional structure with a 2D density $N = 1.117 \times 10^{11}/\text{cm}^2$ corresponding to the same Fermi energy $\varepsilon_F = 4.0$ meV.

The tunneling-current spectra are shown in Fig. 4 for a three-dimensional double-barrier structure with $V_2 = V_4 = 260$ meV, $V_3 = V_5 = 10$ meV, $m_1^* = m_3^* = m_5^* = 0.067 m_0$ and $m_2^* = m_4^* = 0.091 m_0$. The barrier widths are 60 Å. The quantum well width equals 100 Å. A small change in the effective barrier height arising from the effective-mass mismatch at the boundaries for a finite transverse momentum is ignored. The spectra at $T = 0$ K show three resonance peaks for both $n = 2 \times 10^{16}$ and $8 \times 10^{16}/\text{cm}^3$. The two major peaks just below $\hbar\omega = 40$ and 130 meV are due to one-photon-assisted tunneling through the two lowest resonance levels of the quantum well, while the weak peaks near 20 meV are due to two-photon-assisted tunneling through the first resonance level. There are tiny peaks near 65 meV barely visible in Fig. 4. These peaks are due to two-photon-assisted tunneling through the second resonance level. Higher-order contributions are negligible. The peaks for $n = 8 \times 10^{16}/\text{cm}^3$ are wider and lower in energy than those for $n = 2 \times 10^{16}/\text{cm}^3$ because the Fermi energy ($\varepsilon_F = 10.1$ meV) is larger. The widths of the peaks equal approximately the Fermi energies and increase with n as $n^{2/3}$, while the current rises linearly with n approximately. The thermionic current dominates at $T = 77$ K and above as shown by the dashed curve. The oscillations of the curves are due to numerical fluctuations. The inset shows the activation behavior of the current for the zero-photon case. The slopes in the region $0.01 < 1/T$

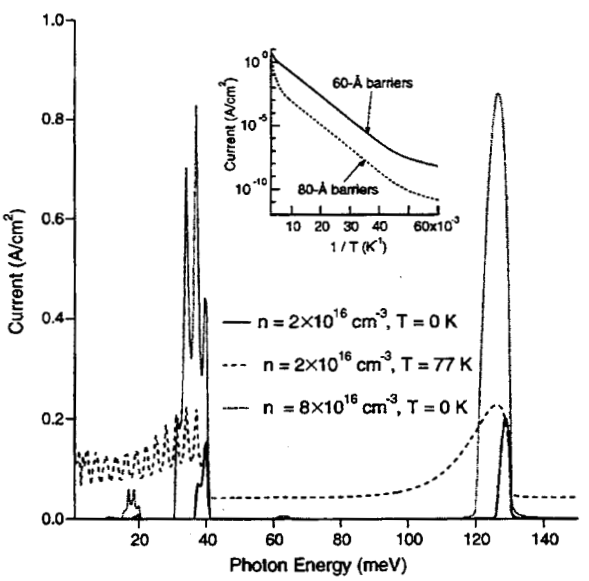

FIG. 4. Transmission-current spectra of the double-barrier structure described in the text. The inset shows the activation behavior of the thermionic current without photons for the same structure (solid curve) and with 80-Å-wide barriers (dotted curve).

$<0.05\,K^{-1}$ correspond to the activation energy to the first resonance level in the quantum well. Similar spectra are obtained for a two-dimensional structure (with $N=1.117\times10^{11}/cm^2$ and the same $\varepsilon_F=4.0$ meV) showing the same resonance energies as in Fig. 4 and similar 2D-3D ratio of the magnitudes of the current as in Fig. 3.

III. SUMMARY

In summary, we have studied multiphoton-assisted activation and transmission of electrons through single-step, single-barrier and double-barrier potential-energy structures as a function of the photon energy, temperature, and the barrier height. Sharp resonances in the tunneling current may have valuable applications for infrared detectors.

ACKNOWLEDGMENTS

The author thanks Dr. J. A. Simmons for many indispensable discussions about IR devices. He acknowledges very helpful discussions on quantum scattering with Dr. M. E. Riley. Sandia is a multiprogram laboratory operated by Sandia corporation, a Lockheed Martin Company, for the U.S. DOE under Contract No. DE-AC04-94AL85000.

[1] T. C. L. G. Sollner, W. D. Goodhue, P. E. Tannenwald, C. D. Parker, and D. D. Peck, Appl. Phys. Lett. **43**, 588 (1983).

[2] L. P. Kouwenhoven, S. Jauhar, J. Orenstein, P. L. McEuen, Y. Nagamune, J. Motohisa, and H. Sakaki, Phys. Rev. Lett. **73**, 3443 (1994).

[3] B. J. Keay, S. J. Allen, Jr., J. Gala'n, J. P. Kaminski, K. L. Campman, A. C. Gossars, U. Bhattacharya, and M. J. W. Rodwell, Phys. Rev. Lett. **75**, 4098 (1995).

[4] H. Drexler, J. S. Scott, S. J. Allen, Jr., K. L. Campman, and A. C. Gossard, Appl. Phys. Lett. **67**, 2816 (1995).

[5] P. K. Tien and J. P. Gordon, Phys. Rev. **129**, 647 (1963).

[6] P. Johansson, Phys. Rev. B **41**, 9892 (1990).

[7] J. Iñarrea, G. Platero, and C. Tejedor, Phys. Rev. B **50**, 4581 (1994).

[8] C. A. Stafford and N. S. Wingreen, Phys. Rev. Lett. **76**, 1916 (1996).

[9] M. H. Pedersen and M. Büttiker, Phys. Rev. B **58**, 12 993 (1998).

[10] G. Burmeister and K. Maschke, Phys. Rev. B **57**, 13 050 (1998).

[11] M. Wagner, Phys. Rev. Lett. **76**, 4010 (1996).

Appendix V. "Terahertz Photoconductivity and Plasmon Modes in Double Well Field Effect Transistors"

Terahertz photoconductivity and plasmon modes in double quantum well field effect transistors.

X. G. Peralta, S. J. Allen
Center for Terahertz Science and Technology, University of California, Santa Barbara, California 93106

N. E. Harff, M. C. Wanke, M. P. Lilly, J. A. Simmons, J. L. Reno
Sandia National Laboratories, Albuquerque, New Mexico 87185

P. J. Burke, J. P. Eisenstein
Department of Physics, California Institute of Technology, Pasadena, California 91125

Double quantum well field effect transistors with a grating gate exhibit resonant, voltage tuned terahertz photoconductivity. The resonant frequency is determined by the 2-dimensional plasma oscillations of the composite structure and is directly related to the electron densities of the wells and the period of the grating. These results suggest that this type of device could be developed into a fast, tunable terahertz detector.

Double quantum well heterostructures have been important in the scientific exploration of correlated electron states in 2-dimensional electron systems[1] and potentially important for novel field effect transistors that add functionality by controlling electron transfer between the quantum wells.[2] Interwell transfer can also be promoted by terahertz photon assisted tunneling between the quantum wells, opening the possibility of fast, voltage tunable terahertz detectors.[3] We report the terahertz photoconductivity of double quantum well field effect devices in which the gate is a periodic metallic grating. Strong photo-response occurs at the plasma resonance, which is controlled by both the voltage applied to the gate and the period of the grating.

Recently, there have also been proposals to fabricate detectors for the terahertz range that make use of plasmon modes in single two-dimensional electron gas (2DEG) systems.[4] But, the relatively strong resonant response that we report here appears to require the presence of a double quantum well. We model the resonant response with a transmission line model of the collective modes of the 2DEG under the metalization and correlate the observed resonances with standing plasmon resonances under the metallic part of the grating gate. These results suggest that this device could be developed into a detector based on plasmon modes in 2DEG bilayer systems.

The field effect devices are fabricated from modulation doped GaAs/AlGaAs double quantum well heterostructures grown on a semi-insulating GaAs substrate by molecular beam epitaxy. Both quantum wells are 200 wide and are separated by a 70 barrier. The nominal electron densities in the quantum wells are $n_{upper}=1.7\times10^{11}cm^{-2}$ and $n_{lower}=2.57\times10^{11}$ cm^{-2}: the 4.2K mobility is $\sim1.7\times10^{6}$ cm^2/Vs. A 2x2mm mesa is defined by wet chemical etching and NiAuGe ohmic contacts to both quantum wells form the source and drain. A 700 thick TiAu grating gate is evaporated with the lines of the grating parallel to the ohmic contacts, perpendicular to the current flow. Grating periods of 4 and 8 μm were explored where half the period is metal. The grating serves to 1) modulate the electron density in the quantum wells by acting as a gate, 2) produce a component of the terahertz electric field normal to the layers and 3) select the wavevectors of the excited plasmon. A cross section of the sample is shown in the inset of FIG. 1.

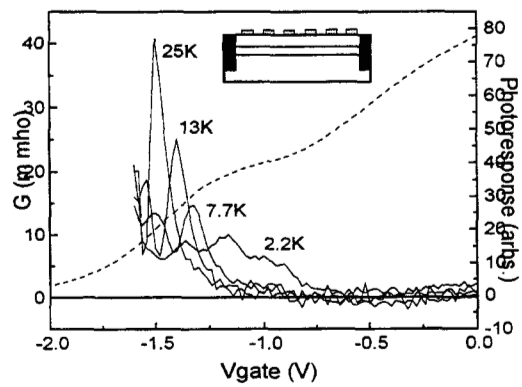

FIG. 1. Source-drain conductance as a function of gate voltage (dashed). Terahertz photoreponse at 570 GHz at four different temperatures (solid). Grating period is 4 μm. Schematic cross section of the devices (inset).

To measure the terahertz photoresponse, the samples are wire bonded and mounted onto a fiberglass chip carrier inside a variable temperature cryostat. Radiation is focused onto the sample with and off-axis parabolic mirror. We apply a constant source-drain current of 100μA and study the photoconductive response of the double quantum wells as a function of gate voltage, terahertz frequency and temperature. The radiation sources are the free-electron lasers at UCSB, which cover a frequency range between 120 GHz and 4.8 THz. Results were obtained in the low power limit by assuring that the response was a linear function of incident power.

FIG. 1 shows the conductance of the double quantum well channels as a function of gate voltage (depletion curve)

as well as the photoconductive response at four different temperatures at a frequency of 570 GHz for the 4μm grating period sample. The depletion curve shows that at Vg~-0.80V the top 2DEG has been fully depleted under the metallic portion of the grating gate forming an array of disconnected 2μm stripes, therefore the current is mainly flowing in the lower 2DEG. As the gate voltage increases, the lower 2DEG is also patterned into stripes and, eventually, the conductance of the double layer system goes to zero when both layers are cut off from the source and drain contacts.

The photoresponse at 570 GHz shows a broad structured peak at Vg~-1.19V at T=2.2K. This feature increases and narrows as a function of increasing temperature. This trend continues up to around T=40K after which the response decreases. At T=80K it is back down to the size it had at T=2.2K. The temperature dependence is unexplained at this time.

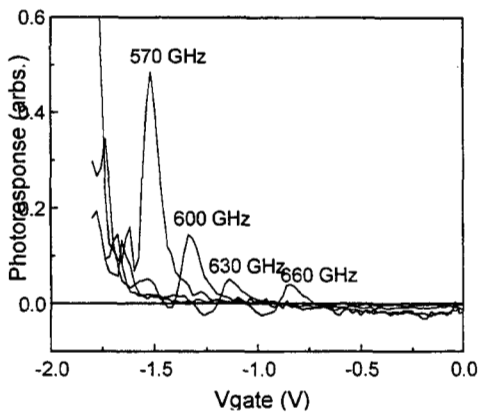

FIG. 3. Terahertz photoresponse as a function of gate voltage at four different frequencies. The temperature was T=25K and the source-drain current was I_{SD}=100μA. Grating period is 4μm.The peak positions follow the bilayer plasmon dispersion relation.

FIG. 3 shows the gate dependent photoresponse at T=25K as a function of radiation frequency for the same sample. The resonant peak moves to lower gate voltage, higher electron density, as we increase the frequency of the incident radiation. This follows the expected dispersion relation for plasmon modes in 2DEG systems. The response is linear with respect to the incident power, as mentioned earlier, and with respect to source-drain current (it is photoconductive, not photovoltaic) in the region studied. In order to ascertain that this response comes from having two 2DEGs, we also measured the photoresponse of a single 2DEG processed in an identical manner and saw no similar behavior.

The dependence on grating period was determined with a sample made of the same double quantum well material and processed in the same way but with an 8 μm grating period. FIG. 4 shows the photoresponse at 600 GHz as a function of gate voltage at T=25K for both the 4 and the 8 μm periods. One can observe multiple resonances in the photoresponse for the 8 μm period.

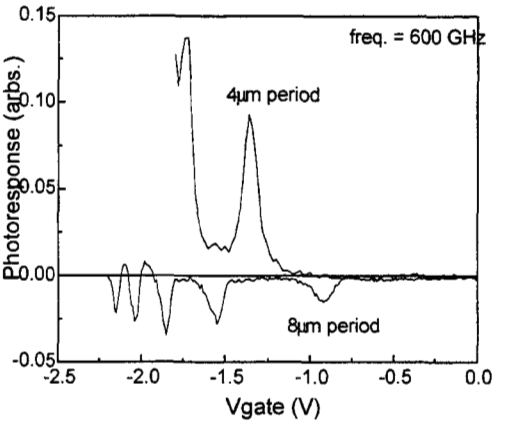

FIG. 4. Terahertz photoresponse at 600 GHz for two samples with different grating periods: 4 and 8 μm at T=25K. Observe the multiple resonances in the 8μm period sample.

As further corroboration, we constructed a simple model that captures the essential physics of the problem.[5] It is well known that a bilayer system of two dimensional electron gases has two plasmon modes that correspond to the charge density oscillations in each layer being in-phase (optic plasmon) and out-of-phase (acoustic plasmon). These modes have been studied both theoretically[6,7] and experimentally.[8,9,10,11] But to find the resonance response here, we model the collective response of the composite structure by combining the sheet densities of the two quantum wells into one ($n_{effective} = n_{upper} + n_{lower}$). In this way we ignore the bilayer acoustic mode.

The standing waves under the grating metal are modeled by a transmission line with a variable density 2DEG (ranging from $n_{effective}$ to zero). The effective impedance of the gated region is added in series with the impedance of the ungated region with a fixed density 2DEG ($n_{effective}$). (See lower right hand side inset in FIG. 5.) In this way we can calculate the ratio of the absorbed power to the incident power as a function of the electron density under the grating metalization, which is controlled by the gate voltage. The lower plot in FIG. 5 shows the resulting normalized absorption as a function of gate voltage for the corresponding frequencies used in the experiment. The upper plot shows the plasmon wavevector at a particular frequency as a function of gate voltage. The horizontal lines correspond to an odd integer number of plasmon wavelengths underneath the metal. The first set of resonances in the normalized absorption (from right to left) correspond to the plasmon with wavevector $3q=3*(2\pi/4\mu m)$, as indicated by the parallel vertical lines, and the second to $5q=5*(2\pi/4\mu m)$.

The insets on the top right are a schematic representation of the current density distribution under the metal gate for the corresponding resonant modes. The resonant peak moves to lower gate voltage, higher electron density, as we increase the frequency of the radiation just as it does in the experiment.

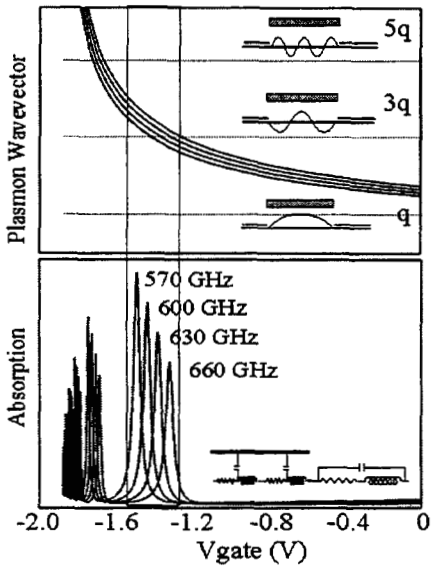

FIG. 5. Top: Plasmon wavevector as a function of gate voltage, with frequency as a parameter. Horizontal lines correspond to odd integer number of plasmon _ wavelengths. Schematic representation of plasmon modes underneath the metal (inset). Bottom: Normalized absorption as a function of gate voltage for the frequencies used in the experiment obtained from the transmission line model described in the text. Element of the transmission line model (inset).

From FIG. 3 we can see that this device can be used as a tunable detector. In that spirit we made an estimate of its noise equivalent power and found NEP=50μW/Hz$^{1/2}$ and we found a responsivity of R=100μV/W. At present, this is not competitive with good incoherent detectors. On the other hand the response time has been measured to be no slower than 700 nsec. If the speed is sufficiently fast, it may find use as a THz heterodyne detector integrated with IF electronics.

In conclusion, we have observed a resonant photoresponse in a 2DEG bilayer system corresponding to the excitation of standing plasma waves under the metallic part of a grating gate. There are several issues that remain to be addressed - the temperature dependence of the amplitude and linewidth, the sign reversal with grating period, and lineshape variation with frequency.

While we understand that the tunable resonance is caused by the composite plasma oscillations, the mechanism that gives rise to the change in conductance at resonance is not understood. It is conditioned on the presence of the bilayer: a single 2-DEG does not respond this way. An in-plane magnetic field produces striking effects (to be presented elsewhere) that support the conclusion that coupled double quantum wells are necessary.

The authors would like to thank D. Enyeart and G. Ramian at the Center for Terahertz Science and Technology. This work was supported by the ONR MFEL program, the DARPA/ONR THz Technology, Sensing and Satellite Communications Program and the ARO, Science and Technology of Nano/Molecular Electronics: Theory, Simulation, and Experimental Characterization.

[1] J. P. Eisenstein, L. N. Pfeiffer and K. W. West, Appl. Phys. Lett **58**, 1497 (1991).

[2] J. A. Simmons, M. A. Blount, J. S. Moon, S. K. Lyo, W. E. Baca and M. J. Hafich, J. Appl. Phys. **84**, 5626 (1998); J. S. Moon, J. A. Simmons, M. A. Blount, W. E. Baca, J. L. Reno and M. J. Hafich, Elect. Lett. **34**, 921 (1998).

[3] B. J. Keay, S. Zeuner, S. J. Allen, K. D. Maranowski, A. C. Gossard, U. Bhattacharya and M. J. W. Rodwell, Phys. Rev. Lett. **75**, 4102 (1995); H. Drexler, J. S. Scott, S. J. Allen, K. L. Campman and A. C. Gossard, Appl. Phys. Lett. **67**, 2816 (1995).

[4] M. S. Shur and J.-Q. Lu, IEEE Trans. Microwave Theor. Tech. **48**, 750 (2000); V. Ryzhii, I. Khmyrova, and M. Shur, J. Appl. Phys. **88**, 2868 (2000).

[5] P. J. Burke, private communication (1998).

[6] S. Das Sarma and A. Madhukar, Phys. Rev. B **23**, 805 (1981).

[7] G.E.Santoro and G. F. Giuliani, Phys. Rev. B **37**, 937 (1981).

[8] N. P. R. Hill, J. T. Nicholls, E. H. Linfield, M. Pepper, D. A. Ritchie, G. A. C. Jones, B. Y.-K. Hu, and K. Flensberg, Phys. Rev. Lett. **72**, 1506 (1994).

[9] A. S. Bhatti, D. Richards, H. P. Hughes, E. H. Linfield, D. A. Ritchie, G. A. C. Jones, in *Proceedings of 23rd International Conference on the Physics of Semiconductors*, edited by M. Scheffler and R. Zimmerman (World Scientific, Singapore, 1996), p. 1899.

[10] D. S. Kainth, D. Richards, A. S. Bhatti, H. P. Hughes, M. Y. Simmons, E. H. Linfield, and D. A. Ritchie, Phys. Rev. B **59**, 2095 (1999).

[11] D. S. Kainth, D. Richards, H. P. Hughes, M. Y. Simmons, and D. A. Ritchie, Phys. Rev. B **57**, R2065 (1998).

Distribution:

1	MS 1427	Org. 1100	J. M. Phillips
1	MS 1415	Org. 1110	W. B. Gauster
2	MS 1421	Org. 1120	G. A. Samara
1	MS 1413	Org. 1040	T. A. Michalske
5	MS 0601	Org. 1123	J. A. Simmons
1	MS 1415	Org. 1123	S. K. Lyo
1	MS 0601	Org. 1113	J. L. Reno
1	MS 1415	Org. 1113	M. P. Lilly
1	MS 0614	Org. 2522	W. E. Baca
1	MS 1077	Org. 1740	T. E. Zipperian
1	MS 0603	Org. 1743	B. K. Smith
1	MS 0603	Org. 1743	J. R. Wendt
1	MS 0603	Org. 1743	M. C. Wanke
1	MS 9018	Org. 8945-1	Central Technical Files
2	MS 0899	Org. 9616	Technical Library
1	MS 0612	Org. 9612	Review & Approval Desk for DOE/OSTI
2	MS 0188	Org. 1030	LDRD Office